

Disc fragmentation and oligarchic growth of protostellar systems in low-metallicity gas clouds

Gen Chiaki^{1*} and Naoki Yoshida^{2,3,4}

¹Center for Relativistic Astrophysics, School of Physics, Georgia Institute of Technology, Atlanta, GA 30332, USA

²Department of Physics, School of Science, The University of Tokyo, 7-3-1 Hongo, Bunkyo, Tokyo 113-0033, Japan

³Kavli Institute for the Physics and Mathematics of the Universe (WPI), UT Institute for Advanced Study, The University of Tokyo, Kashiwa, Chiba 277-8583, Japan

⁴Research Center for the Early Universe (RESCEU), School of Science, The University of Tokyo, 7-3-1 Hongo, Bunkyo, Tokyo 113-0033, Japan

ABSTRACT

We study low-metallicity star formation with a set of high-resolution hydrodynamics simulations for various gas metallicities over a wide range $0\text{--}10^{-3} Z_{\odot}$. Our simulations follow non-equilibrium chemistry and radiative cooling by adopting realistic elemental abundances and dust size distribution. We examine the condition for the fragmentation of collapsing clouds (cloud fragmentation; CF) and of accretion discs (disc fragmentation; DF). We find that CF is suppressed due to rapid gas heating accompanied with molecular hydrogen formation, whereas DF occurs in almost all our simulations regardless of gas metallicities. We also find that, in the accretion discs, the growth of the protostellar systems is overall oligarchic. The primary protostar grows through the accretion of gas, and secondary protostars form through the interaction of spiral arms or the break-up of a rapidly rotating protostar. Despite vigorous fragmentation, a large fraction of secondary protostars are destroyed through mergers or tidal disruption events with other protostars. For a few hundred years after the first adiabatic core formation, only several protostars survive in a disc, and the total mass of protostars is $0.52\text{--}3.8 M_{\odot}$.

Key words: galaxies: evolution — ISM: abundances — stars: formation — stars: low-mass — stars: Population III — stars: Population II

1 INTRODUCTION

The first generations of metal-free Population III (Pop III) stars and metal-poor Population II (Pop II) stars play an important role in the early phase of structure formation. Massive stars ($> 8 M_{\odot}$) can emit ultraviolet (UV) photons and suppress star formation. Whereas, their supernova (SN) explosions can enrich the interstellar medium (ISM) with metals/grains and enhance star formation. The UV emission rate and metal mass depend on the stellar mass. However, the mass range of Pop III and Pop II stars is poorly known.

It has been believed that the transition of the typical stellar mass occurs from massive Pop III stars ($\sim 10\text{--}1000 M_{\odot}$) to low-mass Pop II stars ($\lesssim 1 M_{\odot}$). A metal-free, primordial gas cloud can collapse only slowly for the lack of efficient coolants, and no or little fragmentation occurs until the first protostar forms at the center (Bromm et al. 1999; Abel et al. 2002; Yoshida, Omukai, & Hernquist 2008; Hirano et al. 2014, 2015). In contrast, a gas cloud enriched with

a slight amount of heavy elements is unstable due to radiative cooling of metals/grains. The fragmentation of clouds (*cloud fragmentation*; CF) induced by dust cooling is important for the formation of low-mass stars with metallicities $\gtrsim 10^{-5} Z_{\odot}$ (Omukai 2000; Schneider et al. 2003; Dopcke et al. 2011; Safranek-Shrader et al. 2014; Smith et al. 2015).

Recent numerical studies have revealed that the fragmentation of a circumstellar disc (*disc fragmentation*; DF), may be an important, even a dominant, physical mechanism to produce low-mass stars. At densities $n_{\text{H}} \gtrsim 10^{16} \text{ cm}^{-3}$, the gas becomes optically thick in continuum, and a hydrostatic core (protostar) form. An accretion disc forming around the core is in general gravitationally unstable. Several authors reported that low-mass secondary protostars with masses $\sim 0.1\text{--}1 M_{\odot}$ form both in primordial discs (Clark et al. 2011; Greif et al. 2012; Susa et al. 2014; Hirano & Bromm 2017; Inoue & Yoshida 2020) and in low-metallicity discs with $10^{-6}\text{--}10^{-3} Z_{\odot}$ (Machida & Nakamura 2015; Chiaki et al. 2016).

Interestingly, binary systems with iron abundances (a proxy of metallicities) $[\text{Fe}/\text{H}] < -3$ are discovered with re-

* E-mail: gen.chiaki@physics.gatech.edu

cent stellar radial velocity measurements (Arentsen et al. 2019).¹ Schlaufman et al. (2018) reported an ultra metal-poor star binary, 2MASS J18082002–5104378 with a metallicity $[\text{Fe}/\text{H}] = -4.07$. From its small binary separation (0.2 au), we can speculate that such a system can form through DF because the typical separation of fragments for CF is ~ 10 au (Chiaki et al. 2016) while that for DF is ~ 1 au (Machida & Nakamura 2015; Greif et al. 2012).

Direct numerical simulations would be best-suited to study the fragmentation of a circumstellar disc, but it is still challenging to follow the long-term evolution ($\sim 10^5$ yr) of a protostellar system up to the point when a majority of stars reach their zero-age main-sequence (ZAMS). To connect the “missing link” between the early collapsing phase and the final state of a protostellar system, researchers often employ the following two technical methods. In the first method, called the sink particle technique, dense regions are replaced with Lagrangian particles. The mass of a sink particle is estimated from the amount of gas accreted into a sphere with a certain accretion radius. In the second method, a stiff equation of state (EOS) is assumed in dense regions to prevent further contraction of gas.

With the sink particle method, recent numerical studies have successfully followed the entire evolution of accretion discs (Fukushima et al. 2020; Sugimura et al. 2020), but further complicated modelling is required to reproduce the following processes that control the multiplicity of protostars (e.g. Wollenberg et al. 2020). Mergers of protostars can efficiently suppress the number of protostars (e.g., Susa 2019). A rapidly rotating protostar acquiring angular momentum from accreted gas eventually breaks up into two protostars (Lyttleton 1953; Chandrasekhar 1962, 1965; Eriguchi et al. 1982). With the stiff EOS method, although we can follow only ~ 10 – 100 yrs of the evolution even with currently available computational resources (Greif et al. 2012; Machida & Nakamura 2015; Hirano & Bromm 2017), this method can accurately reproduce the relevant physical processes, such as mergers and the break-up of protostars.

In the present paper, we perform high-resolution simulations to study the evolution of star-forming gas clouds and accretion discs for a wide range of gas metallicities 0 – $10^{-3} Z_{\odot}$. As in our previous paper (Chiaki et al. 2016, hereafter C16), we adopt metal and dust abundances and the dust size distribution obtained from nucleosynthesis and nucleation models for a Pop III SN (Umeda & Nomoto 2002; Nozawa et al. 2007). Our numerical model consider all relevant radiative cooling processes and chemical reactions together with grain chemistry. With a stiff EOS, we follow the detailed evolution of protostellar systems in the early accretion phase of over a few hundred years. The structure of the paper is as follows. In Section 2, we describe our nu-

Table 1. Properties of minihalos

| Halo | z_{form} | R_{vir} [pc] | M_{vir} [M_{\odot}] | $M_{\text{vir, dm}}$ [M_{\odot}] | $M_{\text{vir, ba}}$ [M_{\odot}] |
|------|-------------------|--------------------------|-------------------------------------|---|---|
| A | 15.15 | 37.5 | 9.7×10^4 | 8.1×10^4 | 1.6×10^4 |
| B | 20.46 | 26.5 | 1.6×10^5 | 1.4×10^5 | 2.0×10^4 |

Note — z_{form} is the formation redshifts. R_{vir} and M_{vir} are the virial radius and mass, respectively. $M_{\text{vir, dm}}$ and $M_{\text{vir, ba}}$ are the virial mass of the dark matter and baryon components, respectively.

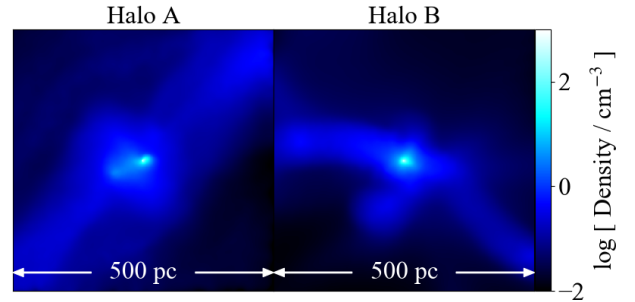


Figure 1. Density-weighted density projections of Halo A and B along the computational z -axis when the maximum density is $n_{\text{H, max}} = 10^3 \text{ cm}^{-3}$. Throughout this paper, we generate projected maps by integrating the contribution of cell-generating points using a cubic spline kernel with a smoothing length of four times the effective cell radius (see text).

merical method and chemical models. Section 3 shows the results of the simulations. We discuss the limitations of our simulations in Section 4 and conclude this paper in Section 5.

2 NUMERICAL MODELS

We perform high-resolution simulations using a moving-mesh/ N -body code AREPO (Springel 2010). We use two small-mass halos (minihalos; MHs) extracted from a parent cosmological simulation of Hirano et al. (2014). We inject metals into gas clouds hosted by the halos and follow their condensation until the gas density reaches $n_{\text{H}} \sim 10^{16} \text{ cm}^{-3}$. Instead of using sink particles, we assume a stiff EOS in dense regions to prevent further collapse and density increase.

2.1 Simulation setup

In AREPO, gravitational force is calculated with a tree method. The gravitational softening length for dark matter particles is fixed to 1.14 pc in all our simulations. For the gas component, each computational cell is defined by the Voronoi diagram. The physical quantities of a gas cell are calculated with a finite-volume method and updated with the fluxes across the cell boundaries. The gravity softening length of a gas cell i is $2.8\Delta x_i$, where $\Delta x_i = (3m_i/4\pi\rho_i)^{1/3}$ is the effective cell radius, and m_i and ρ_i are mass and density of a cell i , respectively.

¹ The abundance ratio of an element A to B is conventionally written as

$$[A/B] = (A(A) - A(B)) - (A_{\odot}(A) - A_{\odot}(B))$$

where

$$A(A) = 12 + \log(y_A)$$

is the absolute abundance of A, and y_A is the number abundance of A relative to hydrogen nuclei. Throughout this paper, we use the solar abundance $A_{\odot}(A)$ of Asplund et al. (2009).

The parent cosmological simulation of Hirano et al. (2014) is carried out with SPH/ N -body simulation code GADGET-2 (Springel 2005). The simulation box size is $1h^{-1}$ comoving Mpc, and the standard Λ CDM cosmology is adopted (Komatsu et al. 2011). The regions of star-forming gas clouds are zoomed-in progressively, and the resulting DM and gas particle masses are $17.3h^{-1} M_{\odot}$ and $3.49h^{-1} M_{\odot}$, respectively.

A total of ~ 100 MHs are identified, out of which we choose two distinctive ones hereafter called Halo A and B.² In C16, we showed that the density structure and fragmentation property depends not only on metallicity but also on the collapsing timescale of clouds. Halo A and B have respectively longest and shortest collapsing timescale $t_{\text{col}} \simeq 10t_{\text{col},0}$ and $\simeq 5t_{\text{col},0}$ among 100 MHs investigated in Hirano et al. (2014), where $t_{\text{col},0} = 1/\sqrt{24\pi G\rho}$ is the e -folding time for the growth of density for an isothermal cloud. We summarize the properties of Halo A and B in Table 1. Halo A collapses at redshift $z_{\text{form}} = 15.15$, and the total mass within the virial radius $R_{\text{vir}} = 37.5$ pc is $M_{\text{vir}} = 9.7 \times 10^4 M_{\odot}$. Halo B forms at redshift 20.46, and its virial radius and mass are $R_{\text{vir}} = 26.5$ pc and $M_{\text{vir}} = 1.6 \times 10^5 M_{\odot}$, respectively. At the formation epoch, we cut out a cubic region around each MH with a side length of 1.15 kpc. The metals and grains are uniformly injected in the entire simulation boxes. The elemental abundance ratios and dust size distributions are taken from Pop III SN models of (Nozawa et al. 2007) as we later describe in Section 2.3.

During the early collapsing phase, the local Jeans length progressively decreases. It is known that spurious fragmentation occurs if a gas element is not sufficiently resolved (Truelove et al. 1997, 1998). To avoid this, we impose the so-called Jeans criterion for cell refinement so that a local Jeans length λ_J is always resolved by more than 32 cells. A cell which violates the criterion is divided into two cells. At density $n_{\text{H}} = 10^{16} \text{ cm}^{-3}$, the minimum mass of a gas cell becomes $\sim 10^{-7} M_{\odot}$ (0.03 Earth masses).

The computational timestep decreases with increasing density. To follow the evolution of an accretion disc after optically-thick protostellar cores form at densities $n_{\text{H}} \gtrsim 10^{16} \text{ cm}^{-3}$, we prevent density increase by switching the adiabatic index γ to

$$\gamma = \begin{cases} 1.4 + 5.2(\log n_{\text{H}} - 16) & \text{for } 16 < \log n_{\text{H}} < 16.5 \\ 4.0 & \text{for } \log n_{\text{H}} > 16.5 \end{cases} \quad (1)$$

for densities above $n_{\text{H,th}} = 10^{16} \text{ cm}^{-3}$ so that γ increases gradually from the value 1.4 for molecular gas to 4.0. The choice of the value 4.0 is motivated from a particular EOS that reproduces the mass-radius relation of protostars (Machida & Nakamura 2015). Hereafter we call a region with densities $n_{\text{H}} > n_{\text{H,th}}$ as a “protostar”.³

Here, we use the time t_* to measure the evolution of

² Halo A is the same as the one used in Chiaki & Yoshida (2015). Halo A and B are the same as MH3 and MH1 in C16, respectively.

³ In reality, at higher densities $n_{\text{H}} \sim 10^{16} - 10^{18} \text{ cm}^{-3}$, gas thermal energy is partly consumed to H_2 dissociation. This chemical gas cooling induces second collapse until all H_2 molecules are consumed. At that time the gas again collapses adiabatically and a hydrostatic core forms. The core hosted by the first core is defined as a protostar (Larson 1969; Penston 1969).

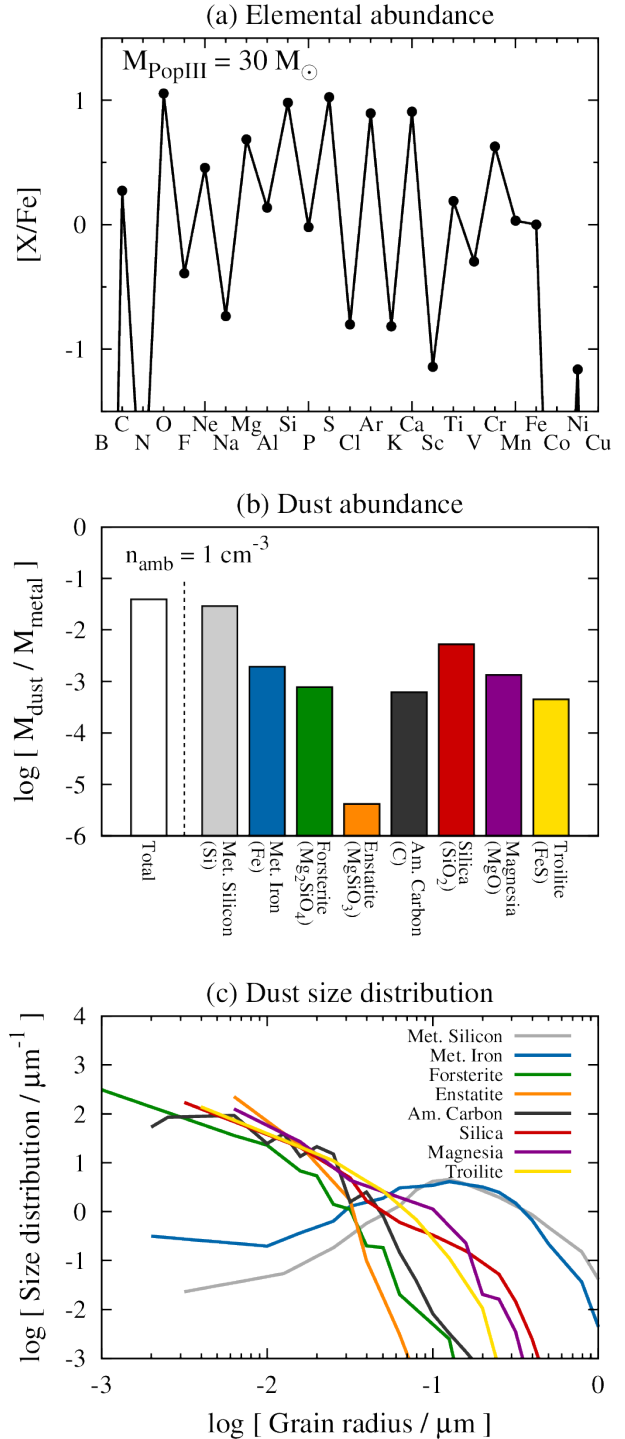


Figure 2. (a) Relative abundance $[X/\text{Fe}]$ of each element X to iron for our Pop III SN model with mass $M_{\text{PopIII}} = 30 M_{\odot}$. (b) Mass fraction of dust grains (white box) and each species (colored boxes) relative to metal for the progenitor model with an ambient gas density $n_{\text{amb}} = 1 \text{ cm}^{-3}$. (c) Size distribution φ_i of each grain species i normalized to unity.

Table 2. Properties of protostellar systems

| Halo | Z [Z_{\odot}] | $t_{*,\text{fin}}$ [yr] | $N_{*,\text{tot}}$ | N_* | $M_{*,\text{tot}}$ [M_{\odot}] | \dot{M}_* [M_{\odot}/yr] | T_* [K] |
|------|------------------------|----------------------------|--------------------|-------|---------------------------------------|--|--------------|
| A | 10^{-3} | 400 | 3 | 3 | 0.521 | 1.30×10^{-3} | 278 |
| | 10^{-4} | 200 | 3 | 3 | 0.567 | 2.83×10^{-3} | 466 |
| | 10^{-5} | 200 | 7 | 3 | 1.03 | 5.16×10^{-3} | 696 |
| | 10^{-6} | 200 | 5 | 3 | 1.41 | 7.04×10^{-3} | 855 |
| | 0 | 200 | 13 | 3 | 2.60 | 1.30×10^{-2} | 1287 |
| B | 10^{-3} | 200 | 2 | 2 | 1.42 | 7.11×10^{-3} | 862 |
| | 10^{-4} | 100 | 10 | 4 | 1.88 | 1.88×10^{-2} | 1647 |
| | 10^{-5} | 100 | 9 | 3 | 1.49 | 1.49×10^{-2} | 1408 |
| | 10^{-6} | 100 | 4 | 1 | 5.62 | 5.62×10^{-2} | 3416 |
| | 0 | 100 | 26 | 5 | 3.77 | 3.77×10^{-2} | 2620 |

Note — $N_{*,\text{tot}}$ is the total number of protostars including destroyed ones during $t_{*,\text{fin}}$. N_* and $M_{*,\text{tot}}$ are the number and the total mass of protostars surviving at the time $t_{*,\text{fin}}$. \dot{M}_* is the average mass accretion rate during $t_{*,\text{fin}}$. The temperature of the accreted gas T_* is calculated from $\dot{M}_* = c_s^3/G$.

a protostellar system. The origin of t_* is the time when the maximum density $n_{\text{H,max}}$ among gas cells first reaches $> n_{\text{H,th}}$. We terminate our simulations at $t_{*,\text{fin}} = 100\text{--}400$ yr depending on the runs (see Table 2). We follow longer evolution for larger metallicity and for Halo A because the accretion timescale is longer.

2.2 Chemistry and cooling

We solve all relevant chemical reactions and radiative cooling/chemical heating processes in a self-consistent manner. We here use a chemistry/cooling library GRACKLE for the usage in general hydro-codes (Smith et al. 2017).⁴ In Chiaki & Wise (2019), we have developed this library by supplying with metal/dust chemistry together with the growth of dust grains (grain growth) by accretion of gas-phase metal molecules onto grains. It includes large chemical reaction networks of 100 reactions of 38 gas-phase species, e, H, H^+ , H_2 , H^- , H_2^+ , D, D^+ , D^- , HD, HD^+ , He, He^+ , He^{2+} , HeH^+ , C^+ , C, CH, CH_2 , CO^+ , CO, CO_2 , O^+ , O, OH^+ , OH, H_2O^+ , H_2O , H_3O^+ , O_2^+ , O_2 , Mg, Al, Si, SiO, SiO_2 , S, and Fe, and 10 grain species, metallic silicon (Si), metallic iron (Fe), forsterite (Mg_2SiO_4), enstatite (MgSiO_3), magnetite (Fe_3O_4), amorphous carbon (C), silica (SiO_2), magnesite (MgO), troilite (FeS), and alumina (Al_2O_3) with their compositions in the parentheses. For the cells with densities $n_{\text{H}} > n_{\text{H,th}}$, we do not update the abundances of chemical species. The abundances of these chemical species are treated as passive scalars. The advection of all chemical species is calculated from fluxes across each cell interface.

2.3 Initial metal/dust properties

In the initial conditions of our simulations, we uniformly inject metals and grains to the gas. This is motivated by recent supernova simulations, where the gas metallicity is almost uniform in enriched clouds within a radius ~ 1 pc

(Smith et al. 2015; Chiaki & Wise 2019; Chiaki et al. 2020). SNe could drive strong turbulence just after their explosion, but the turbulence Mach number is 0.38 when the enriched clouds begin to collapse, comparable to the one before the SN (Chiaki & Wise 2019).

We adopt realistic metal/dust properties (abundances of heavy elements and grain species and dust size distribution) taken from nucleosynthesis and nucleation models of a Pop III SN (Umeda & Nomoto 2002; Nozawa et al. 2007). We assume a progenitor mass $M_{\text{PopIII}} = 30 M_{\odot}$ motivated by recent simulations. The local maximum of Pop III stellar mass distribution is at $30 M_{\odot}$ (Susa et al. 2014; Hirano et al. 2014). Also, the elemental abundance ratios of metal-poor stars best fit with progenitor models with $M_{\text{PopIII}} = 25\text{--}30 M_{\odot}$ (Ishigaki et al. 2018).

Fig. 2a shows the abundances of heavy elements in total of the gas and solid phases. This model reproduces the enhancement of α elements such as O, Mg, and Si, of EMP stars although $[\alpha/\text{Fe}]$ is higher than the typical value of EMP stars (~ 0.4). In this model, the oxygen abundance relative to iron is $[\text{O}/\text{Fe}] = 1.05$. We expect that radiative cooling by O-bearing molecules OH and H_2O affect the cloud fragmentation as suggested by C16. From the relative abundance of carbon to iron $[\text{C}/\text{Fe}] = 0.274$, the stars will be classified to C-normal stars by a definition of C-enhanced metal-poor (CEMP) stars ($[\text{C}/\text{Fe}] > 0.7$; Aoki et al. 2007).

Fig. 2b and c show the initial abundances and size distribution of grain species, respectively, in our progenitor model. In general, grains form in the expanding ejecta at 300 d after an SN explosion. All refractory elements such as Mg, Si, and Fe are locked up into grains as in the local ISM (Nozawa et al. 2003). At $\sim 10^4$ yr after the explosion, reverse shocks start propagating backwards into ejecta. Between the forward and reverse shocks, high energy ions sputter the newly forming grains, and the mass fraction of metals locked up into grains decreases. The efficiency of grain destruction depends on the ambient gas density n_{amb} (Nozawa et al. 2007; Bianchi & Schneider 2007). We here consider the grain destruction model with $n_{\text{amb}} = 1 \text{ cm}^{-3}$ because the typical gas density of a H II region created by a progenitor Pop III

⁴ <https://grackle.readthedocs.io/>.

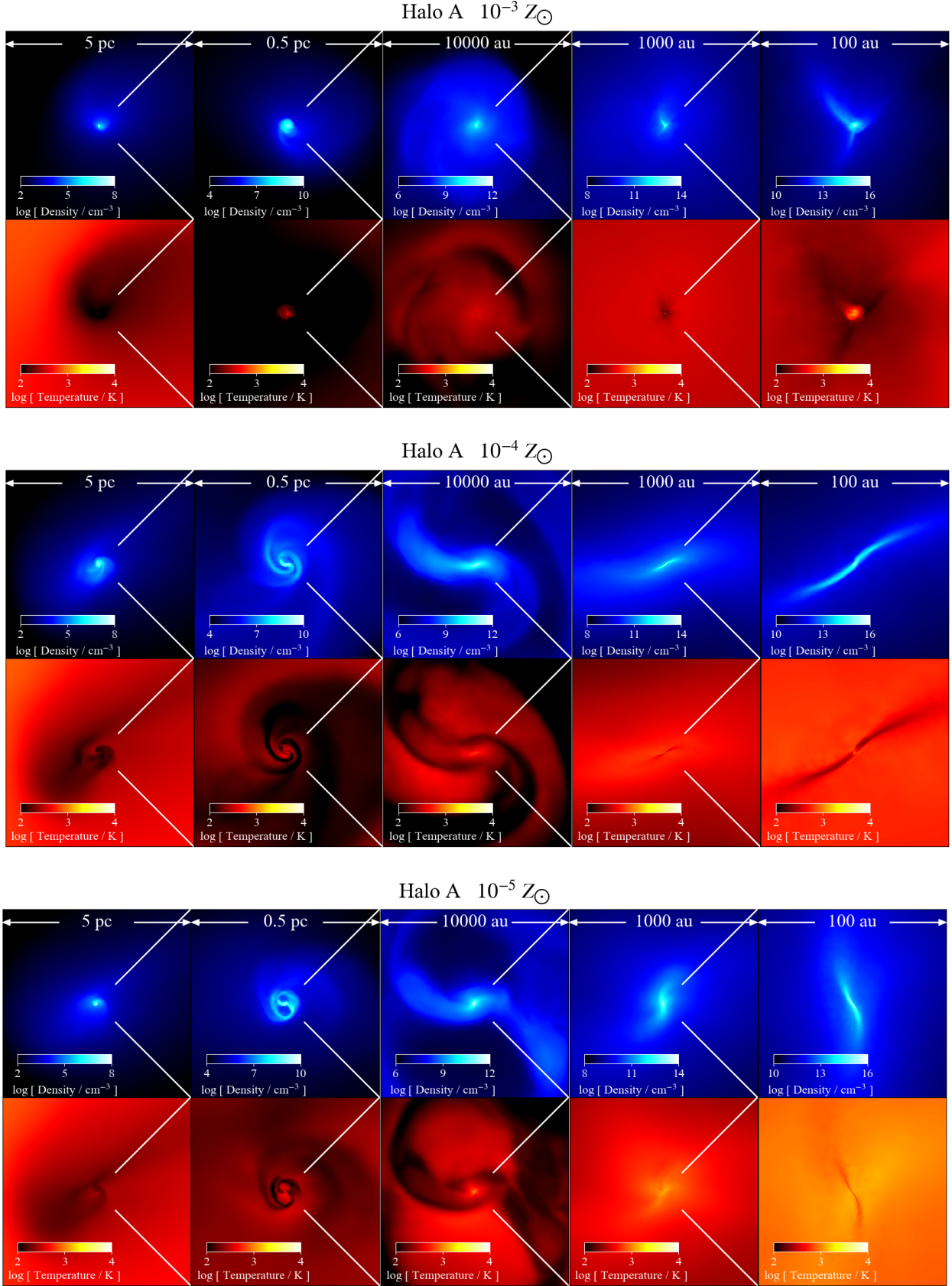
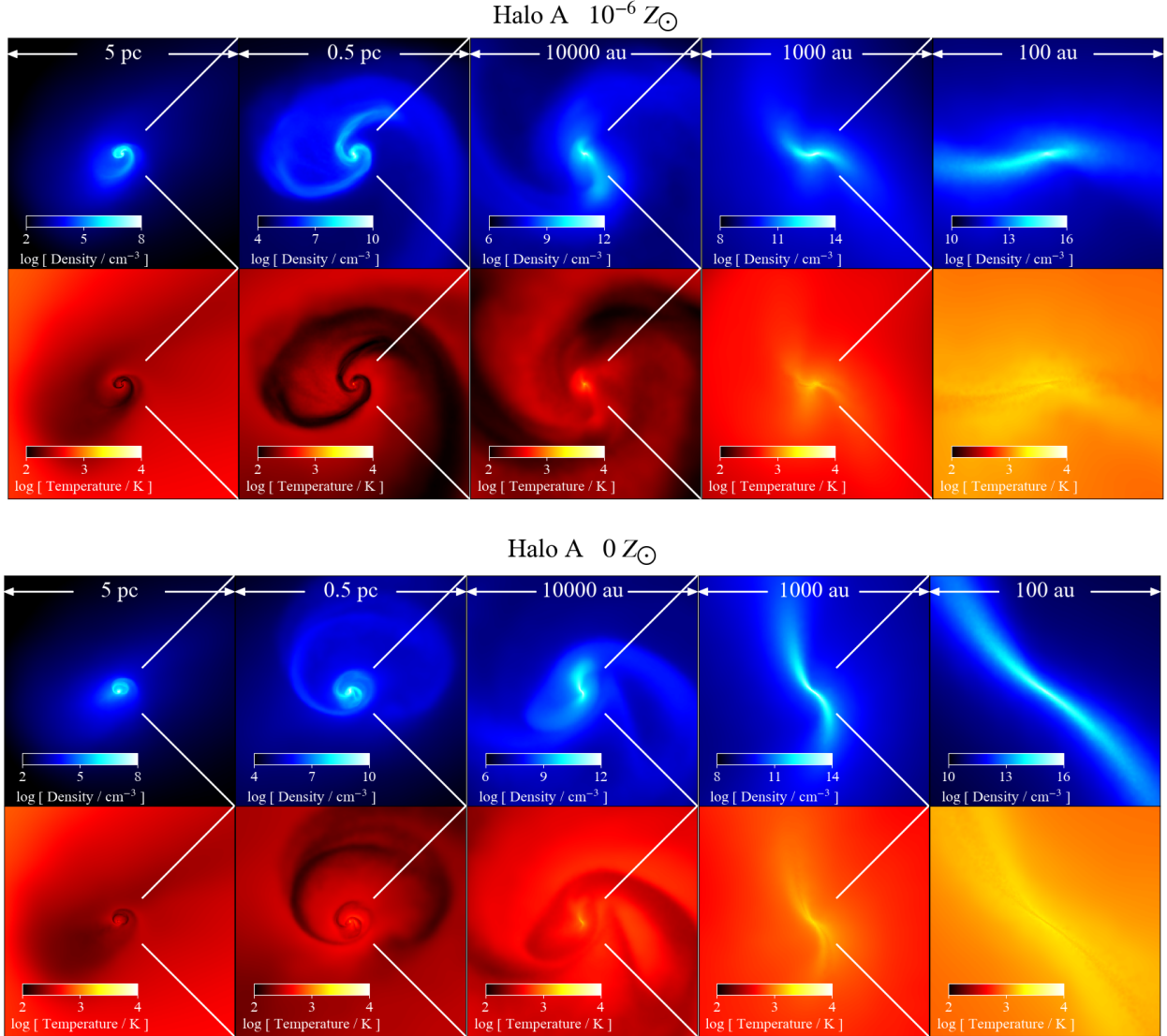


Figure 3. Projections of density and temperature for Halo A when the maximum gas density reaches 10^{16} cm^{-3} along the computational z -axis. We plot the results for metallicities 0 – $10^{-3} Z_{\odot}$ from bottom to top. The size of the zoomed-in area is from 5 pc to 100 au from left to right.

Figure 3. *cont.*

star is $\sim 0.1\text{--}1\text{ cm}^{-3}$ (Kitayama et al. 2004; Whalen et al. 2004, 2008). The dust-to-metal mass ratio is smaller in this model (3.95%) than in the local ISM $\simeq 50\%$ (Pollack et al. 1994).

The absolute amount of metals is given by the total mass fraction of all elements heavier than He. For a metallicity Z , the carbon and iron abundances in our progenitor model are

$$A(\text{C}) = 4.05 + \log \left(\frac{Z}{10^{-4} Z_{\odot}} \right), \quad (2)$$

$$\begin{aligned} [\text{Fe}/\text{H}] &= A(\text{Fe}) - A_{\odot}(\text{Fe}) \\ &= -4.66 + \log \left(\frac{Z}{10^{-4} Z_{\odot}} \right). \end{aligned} \quad (3)$$

The abundance $A(X)$ of an element X is calculated as

$$A(X) = 12 + \log \left(\frac{M_X}{M_{\text{met}}} \frac{Z}{\mu_X X_{\text{H}}} \right), \quad (4)$$

where M_X and M_{met} are mass of X and metals ejected from

the SN, respectively, and μ_X is molecular weight of element X ($\mu_{\text{C}} = 12$ and $\mu_{\text{Fe}} = 56$). We assume the primordial hydrogen mass fraction $X_{\text{H}} = 0.76$ and give metallicities in units of solar metallicity $Z_{\odot} = 0.02$.

Hereafter, our runs with different halos and metallicities are described as the combination of ids of halos {HA, HB} and metallicities {Z0, Z-6, Z-5, Z-4, Z-3}. For example, the run HAZ-4 indicates the run for Halo A and a metallicity $10^{-4} Z_{\odot}$.

3 RESULTS

3.1 Overview

We follow the collapse of clouds hosted by the two MHs and the evolution of accretion disks. When the density of the cloud core reaches $n_{\text{H}} = 10^{16}\text{ cm}^{-3}$, the minimum spatial and mass resolution is $\sim 0.01\text{ au}$ and $\sim 10^{-7} M_{\odot}$, respec-

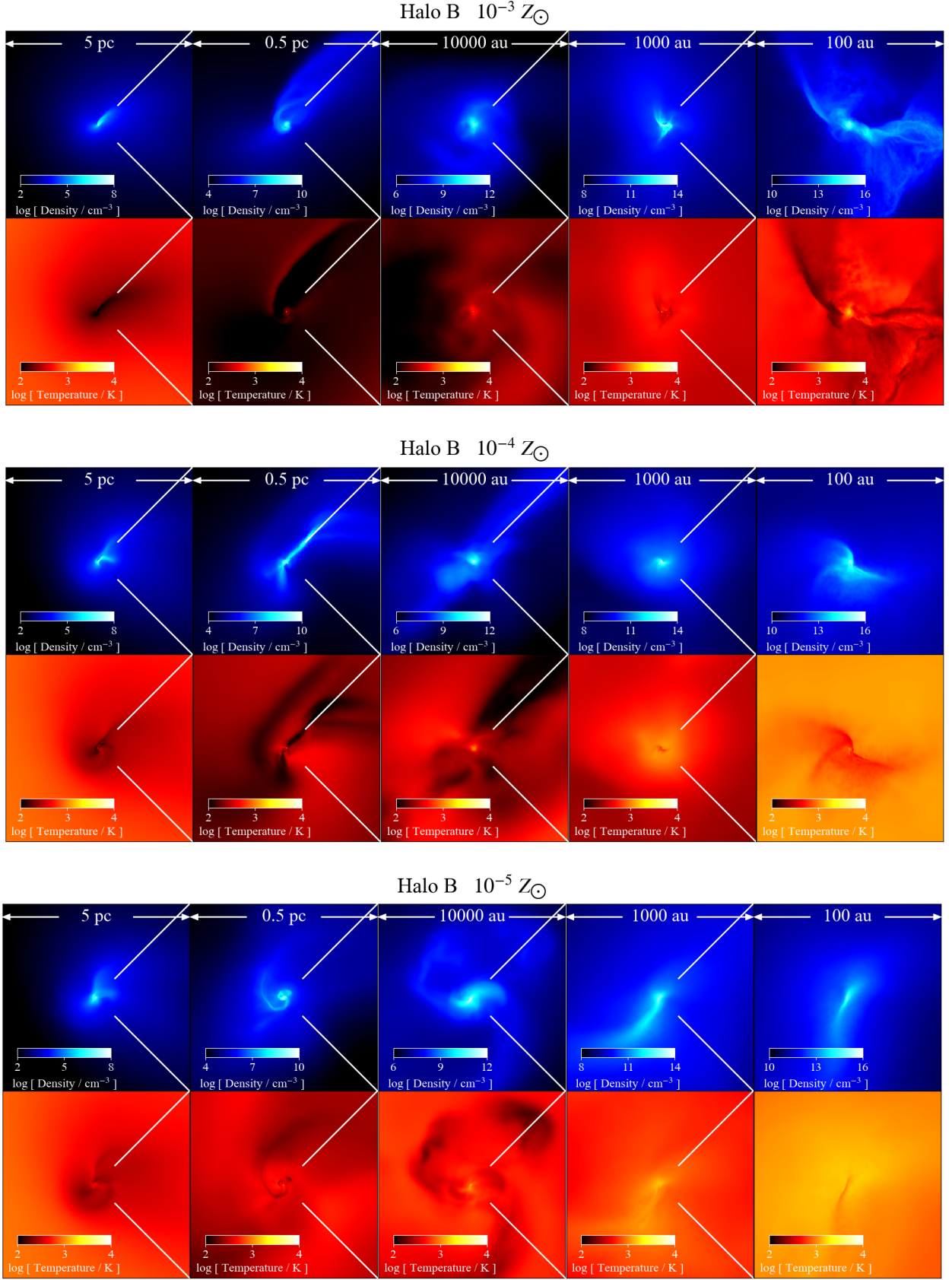
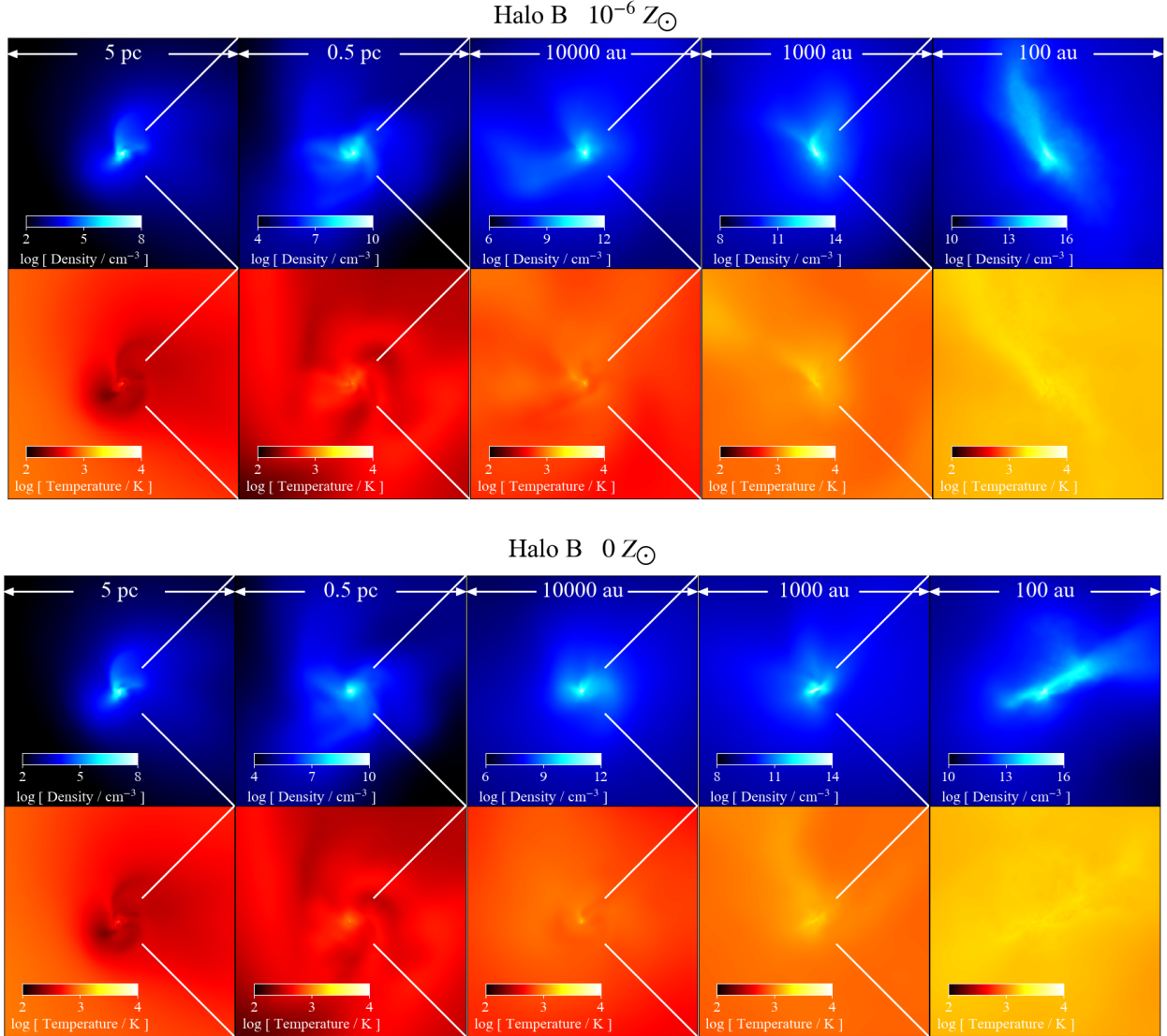


Figure 4. Same as Fig. 3 but for Halo B.

Figure 4. *cont.*

tively. Our simulations resolve protostars with a size of ~ 1 au as seen in Figs. 3 and 4.

Figs. 5 and 6 show the loci of protostars. In the simulations, as many as 26 protostars form, some of which are destroyed within a few 100 yr. The primary protostar grows through gas accretion while secondary protostars form through the break-up of a parent protostar that is strongly deformed by the centrifugal force, or through the interaction of spiral arms around a massive protostar. Some protostars are destroyed through merger with another protostar. When we terminate our simulations at 100–400 yr after primary protostar formation, 1–5 protostars survive. Table 2 shows the total mass of protostellar system $M_{*,\text{tot}}$. The mass is 0.52–3.8 M_{\odot} depending on the mass accretion rate and metallicity as discussed below in more detail.

3.2 Collapsing phase

A gas cloud collapses and condenses toward the center of the gravitational potential generated by the host dark matter halo. Since cloud deformation and fragmentation are controlled by the thermal evolution of the gas, we first discuss cooling/heating processes and chemical evolution in our simulations. Figs. 7 and 8 show the evolution of the temperature and cooling rates as a function of density. Figs. 9 and 10 show the evolution of species abundances for Halo A and B, respectively. The temperature evolution is different between the two MHs even with the same metallicity. Since the collapsing timescale $t_{\text{col}} = \rho/\dot{\rho}$ is longer for Halo A than for Halo B by a factor of two, the gas temperature is lower with the smaller compressional heating rate. The evolution of chemical species abundances does not significantly differ between the two halos with a fixed metallicity (see Figs 9 and 10) but the thermal evolution notably or significantly differs between the runs with different gas metallicities.

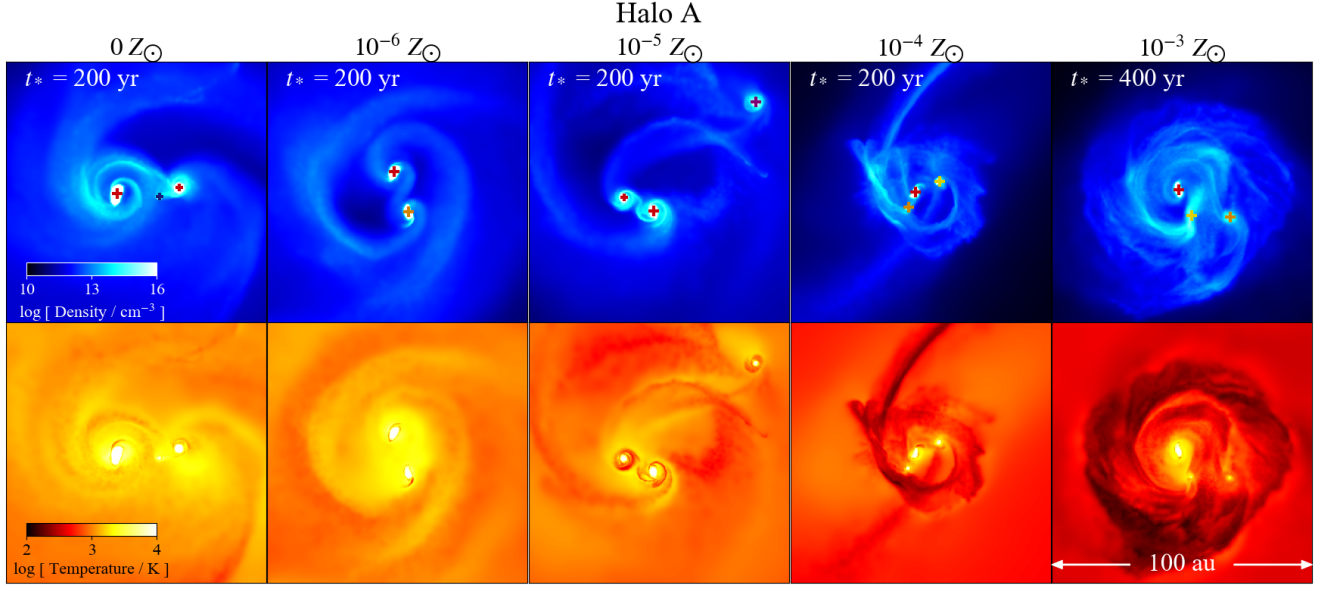


Figure 5. Projections of density (top) and temperature (bottom) in accretion discs for Halo A along the total angular momentum vector of gas with densities $> 10^{14} \text{ cm}^{-3}$ when we terminate the simulations. We plot the results for metallicities $0\text{--}10^{-3} Z_{\odot}$ from left to right. The cross symbols indicate the center of mass of protostars.

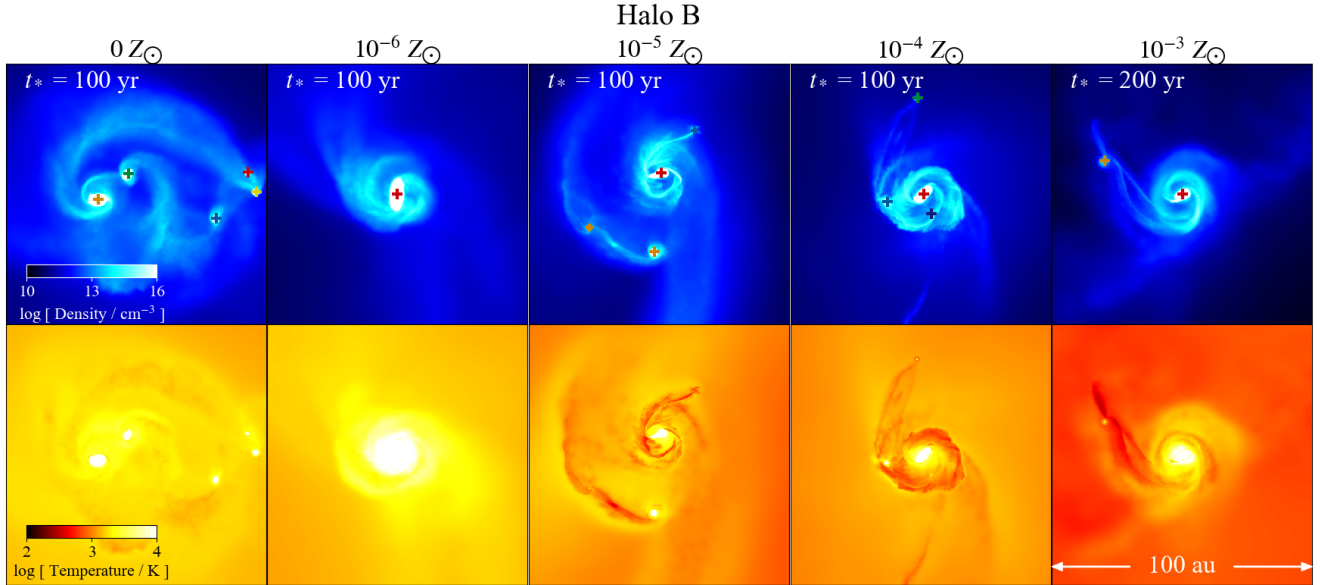
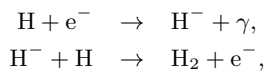


Figure 6. Same as Fig. 5 but for Halo B.

The overall thermal evolution can be described as follows. At low densities $n_{\text{H}} < 1 \text{ cm}^{-3}$, the gas temperature increases adiabatically because none of the cooling processes works efficiently. The hydrogen molecule fraction increases up to $y(\text{H}_2) \sim 10^{-3}$ through the H^- -process as



catalyzed by free electrons. Then, the gas temperature declines by hydrogen molecular cooling. The molecular fraction

increases as metallicity increases because of more efficient molecular formation on grain surfaces. In models where the temperature drops below 150 K, HD molecules form through the reactions



and rotational transition line cooling of HD molecules becomes important.

Metal atoms/ions and molecules also contribute to gas

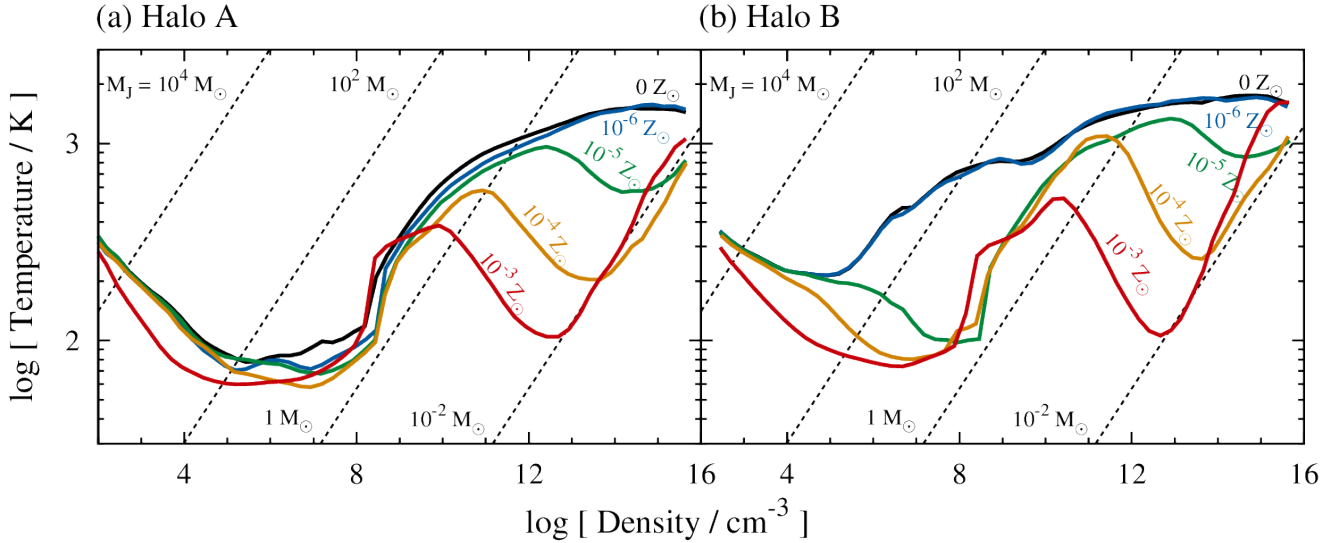
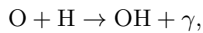


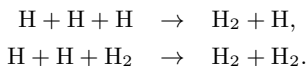
Figure 7. Temperature evolution as a function of maximum density $n_{\text{H,max}}$ in each snapshot for (a) Halo A and (b) Halo B with metallicities 0 (black), $10^{-6} Z_{\odot}$ (blue), $10^{-5} Z_{\odot}$ (green), $10^{-4} Z_{\odot}$ (orange), and $10^{-3} Z_{\odot}$ (red). We dump snapshots at every time when $n_{\text{H,max}}$ increases by 0.25 dex, and calculate the volume-weighted average of density and the mass-weighted average of temperature in a cloud core defined as a region with densities above $n_{\text{H,max}}/3$. The black dotted lines indicate the Jeans mass at the corresponding density and temperature.

cooling. With a metallicity $10^{-3} Z_{\odot}$, fine-structure cooling of O I and rotational transition line cooling of CO become dominant at $n_{\text{H}} \sim 10^2\text{--}10^4 \text{ cm}^{-3}$ and $10^4\text{--}10^6 \text{ cm}^{-3}$, respectively. Since O is dominant over C ($\text{O}/\text{C} > 11$) in our progenitor model, C I and C II fine-structure cooling is inefficient. For metallicities above $10^{-5} Z_{\odot}$, OH molecules form through



and OH cooling becomes dominant. With these molecular cooling, gas temperature reaches CMB temperature of 44 K and 59 K for Halo A and B, respectively, and temperature floor appears in Fig. 7. The nearly isothermal evolution induces cloud deformation (Tsuribe & Omukai 2006; Sugimura et al. 2017). Fig. 3 shows dense ($n_{\text{H}} \sim 10^5\text{--}10^8 \text{ cm}^{-3}$) and cool ($T \simeq 60 \text{ K}$) spiral arms.

The cloud deformation ceases at density $n_{\text{H}} \sim 10^8 \text{ cm}^{-3}$, where efficient gas heating occurs due to the release of binding energy along with hydrogen molecule formation through three-body reactions:



The gas cloud again collapses stably against deformation. The ambient gas is accreted onto the hydrostatic core, and thus the mass and density of the core can continue to increase.

At $n_{\text{H}} \sim 10^{10} (Z/10^{-4} Z_{\odot})^{-2} \text{ cm}^{-3}$, silicate grains start growing by accreting Mg atoms, SiO molecules, and H₂O molecules in the gas phase. Grain growth proceeds until all Mg atoms are eventually depleted (see Figs. 9 and 10). The gas cooling rate due to dust thermal emission is enhanced by grain growth, and the temperature decreases again at densities $n_{\text{H}} \sim 10^{11} (Z/10^{-4} Z_{\odot})^{-1} \text{ cm}^{-3}$ for

metallicities above $10^{-5} Z_{\odot}$. Dust cooling enhances cloud deformation, and the filamentary structure develops. At $n_{\text{H}} \sim 10^{13} (Z/10^{-4} Z_{\odot})^{-1} \text{ cm}^{-3}$, the gas and grains are thermally coupled, and the gas becomes optically thick in continuum. A hydrostatic core forms and accretes mass and angular momentum from ambient gas through spiral arms or filaments.

In C16, we found two distinct density structures that induce CF and DF. Also in this work, we can see a knotty filamentary structure (precursor of CF) for HBZ-3 and spiral arms (precursor of DF) in the other models. In C16, we followed the accretion process only for $< 50 \text{ yr}$ and thus we could not predict whether knotty/clumpy structures survive as secondary protostars or are accreted onto the primary protostars. In order to study the evolution further, we impose a stiff EOS (Eq. 1) to the gas with densities above $n_{\text{H,th}} = 10^{16} \text{ cm}^{-3}$ to follow further mass accretion and fragmentation of the protostellar systems.

3.3 Accretion phase

3.3.1 Accretion discs

In all of our runs, an accretion disc forms around the primary protostar (Figs. 5 and 6). Figs. 11 and 12 show the profiles of density, temperature, and radial velocity as a function of distance from the center of mass of the most massive, primary protostar. To see the three-dimensional properties of the accretion flow, we show the profiles in opposite directions (solid and dashed curves) along the two axes parallel and perpendicular to the angular momentum vector \mathbf{J} (blue and orange curves, respectively). We calculate total angular momentum as $\mathbf{J} = \sum m_i (\mathbf{r}_i \times \mathbf{v}_i)$, where \mathbf{r}_i is the displacement from the center of mass, and \mathbf{v}_i is the relative velocity to the mass-weighted mean velocity among cells with den-

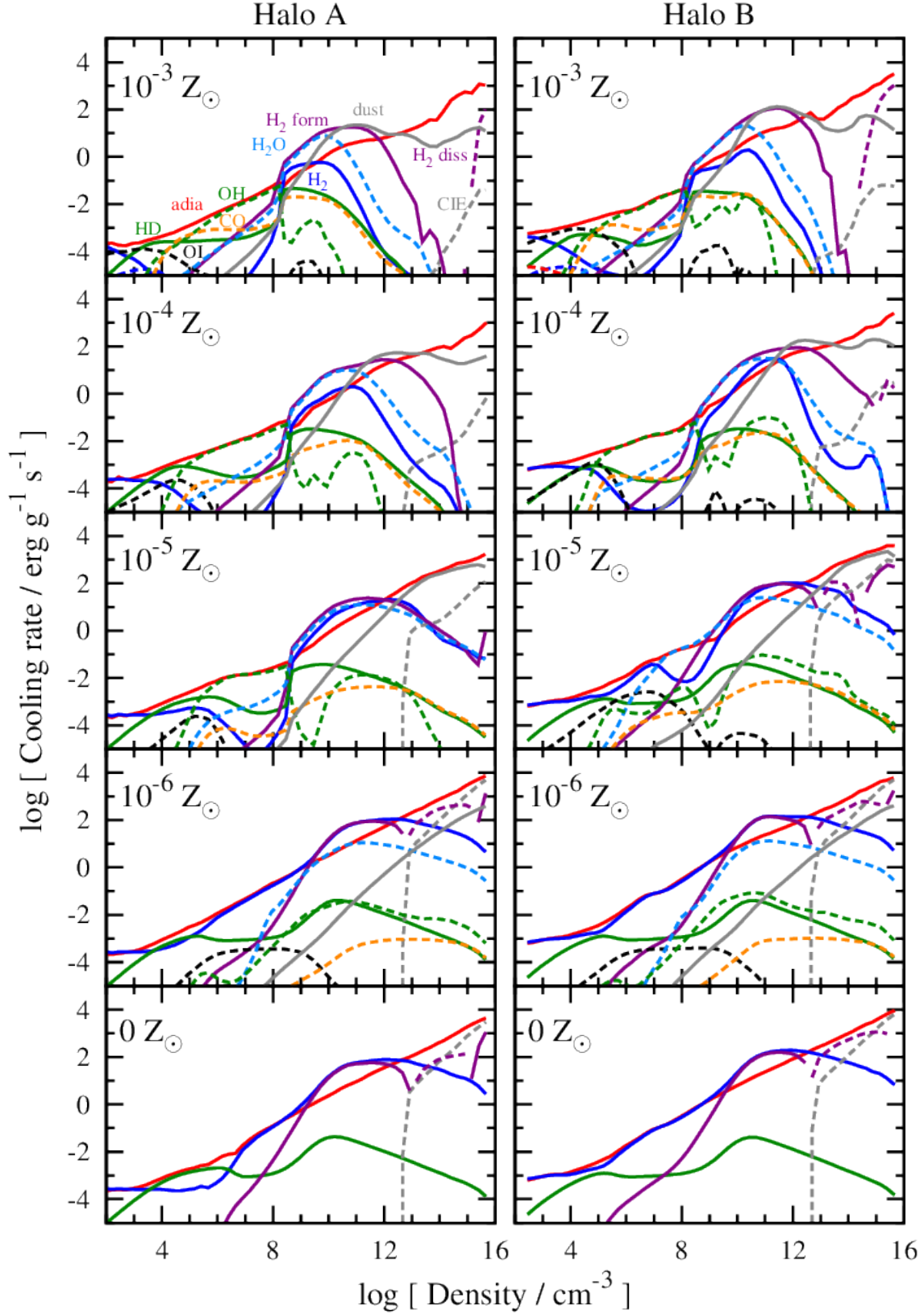


Figure 8. Cooling/Heating rates in cloud cores at each density for Halo A (left panels) and B (right panels) with metallicities 0 – $10^{-3} Z_{\odot}$ from bottom to top. We plot adiabatic heating rate (red solid), H_2 (blue solid), HD (green solid), O I (black dashed), CO (orange dashed), OH (green dashed), H_2O (cyan dashed), H_2 formation cooling (purple solid) and dissociation heating (purple dashed), dust (grey solid), and CIE cooling (grey dashed curve).

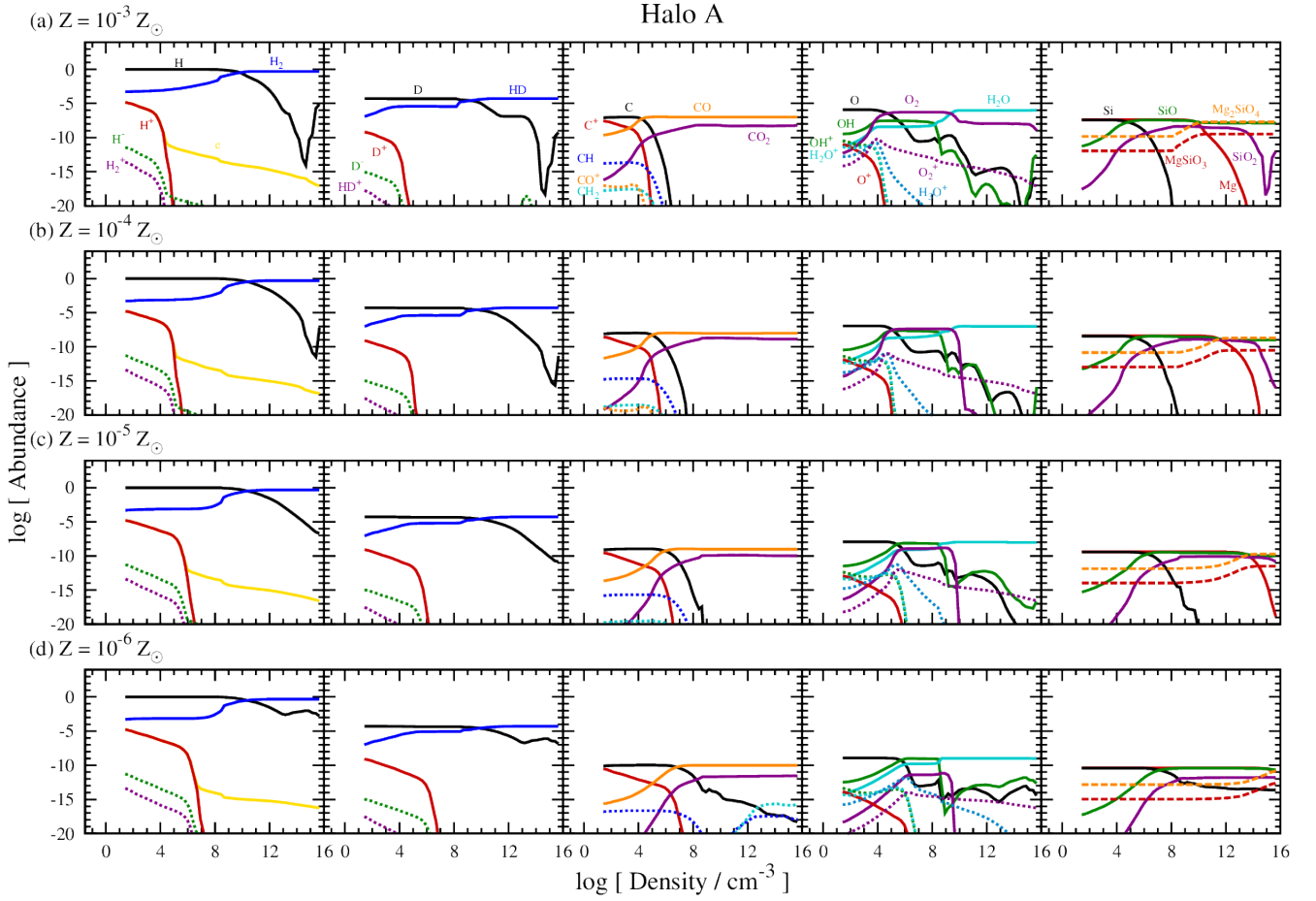


Figure 9. Species abundances relative to hydrogen nuclei in cloud cores at each density for Halo A with metallicities (a) $10^{-3} Z_{\odot}$, (b) $10^{-4} Z_{\odot}$, (c) $10^{-5} Z_{\odot}$, and (d) $10^{-6} Z_{\odot}$. For silicate grains (Mg_2SiO_4 and MgSiO_3), we show the number fraction of Si nuclei locked up into the grains.

sities $> 10^{14} \text{ cm}^{-3}$. Outside the protostar ($\gtrsim 1 \text{ au}$), the density suddenly declines to $\sim 10^{13} \text{ cm}^{-3}$ on the disc plane (orange curves) and $\sim 10^{12} \text{ cm}^{-3}$ on the rotational axis (blue curves). The orange curves show the density plateau in the disc ($\sim 1\text{--}30 \text{ au}$). Along the rotational axis (blue curves), rapid gas accretion occurs with infall velocity $|v_{\text{rad}}| > 10 \text{ km/s}$ because the centrifugal force barrier does not work. Since the infall velocity exceeds the local sound speed, accretion shocks form and the temperature increases to above 10^4 K . For HBZ-6, the disk size is relatively small to the other models, and the gas is accreted onto the protostar in a nearly spherical manner as we discuss in detail in Appendix A3. Because of rapid gas accretion, the gas temperature around the protostar rises up to $\sim 10^5 \text{ K}$ due to compressional heating.

3.3.2 Fragmentation of discs

We find that DF occurs and multiple protostellar systems form in all our runs but for HBZ-6 (Figs. 5 and 6). We identify candidate protostars by employing a friends-of-friends (FOF) algorithm with a threshold density $n_{\text{H,th}} = 10^{16} \text{ cm}^{-3}$ and a linking length $4\Delta x_i$. We count the candidates with mass more than $0.003 M_{\odot}$ ($\sim 3 \text{ Jupiter masses}$)

as protostars. Hereafter, the protostar born in the n 'th order in each run is dubbed as PS n .

Table 2 shows that as many as 26 protostars form until the time $t_{*,\text{fin}}$ when we terminate the simulations. Most of the protostars are destroyed, and only several protostars remain in the accretion disks at $t_{*,\text{fin}}$. The mass evolution of the protostellar systems shows the oligarchic growth.

This is consistent with the results of earlier studies of the evolution of primordial protostellar discs (Clark et al. 2011; Stacy et al. 2012; Greif et al. 2012; Susa 2019). Susa (2019) derived an empirical relationship between the number of protostars and elapsed time t_* as

$$N_* = 3 \left(\frac{\tau_*}{1 \text{ yr}} \right)^{0.3} \quad (5)$$

from earlier studies, where $\tau_* = t_*(n_{\text{H,th}}/10^{19} \text{ cm}^{-3})^{1/2}$ is the scaled time according to the threshold density above which authors assumed that gas becomes adiabatic. With $n_{\text{H,th}} = 10^{16} \text{ cm}^{-3}$ and $t_* = 100\text{--}400 \text{ yr}$, the predicted number of fragments is 4–6, which is consistent with our simulation results in both the metal-free and metal-poor cases.

We also find that the formation of protostars is classified into the following three processes:

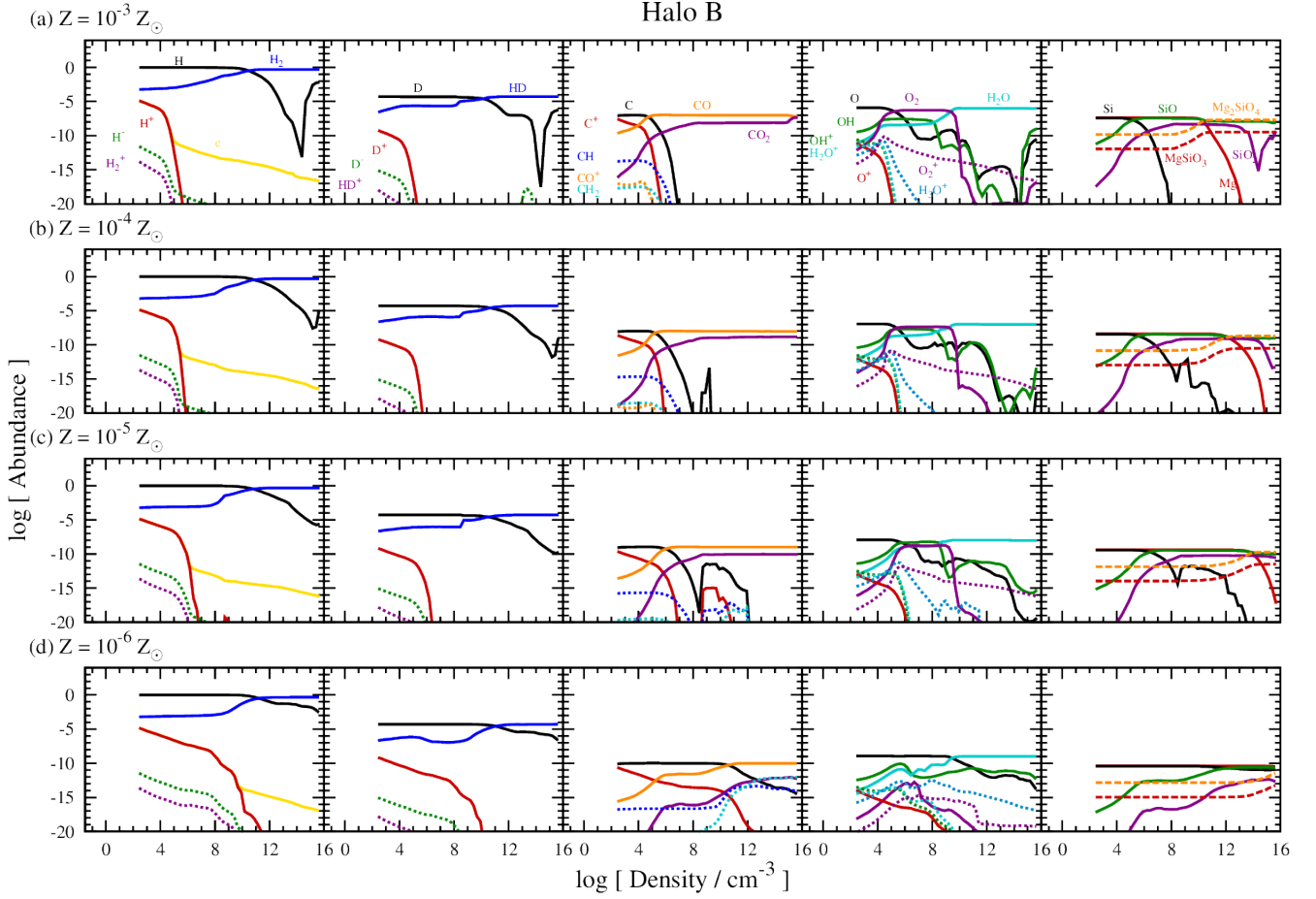


Figure 10. Same as Fig. 9 but for minihalo Halo B.

- (i) gravitational contraction,
- (ii) break-up of rapidly rotating protostars,
- (iii) interaction of spiral arms,

and the destruction of protostars is classified into the following three processes:

- (i) dissolution into ISM
- (ii) mergers with another member protostar,
- (iii) tidal disruption events (TDEs)

as we in detail discuss in Appendix A.

In several runs, although CF occurs initially, accretion discs form and DF occurs eventually. For HBZ-3, cloud deformation is enhanced by dust cooling, and the knotty filamentary structures form (called “filament fragmentation” in C16). Within $t_* = 50$ yr, the filaments are accreted onto PS1 before the density perturbations in the filaments gravitationally grow. Similarly, for HAZ0, HBZ0, and HBZ-6, filament fragmentation occurs, but H_2 cooling induces the fragmentation of filaments in these cases. In all cases, a rotationally supported disc forms quickly after the PS1 accretes a sufficient amount of gas with a finite angular momentum.

3.3.3 Mass evolution of protostars

Table 2 shows the evolution of the total mass of protostars $M_{*,\text{tot}}$. For Halo A, the total mass becomes $0.521\text{--}2.60 M_\odot$ at 200–400 yr after PS1 formation. The values correspond to the mass accretion rates $1.30 \times 10^{-3}\text{--}1.30 \times 10^{-2} M_\odot/\text{yr}$. Assuming that the accretion rate follows a simple scaling $\dot{M}_* \sim c_s^3/G$, the corresponding temperature is 278–1287 K. The mass accretion rate decreases with the increasing metallicity because enhanced molecular and dust cooling reduces the gas temperature around the protostars. For Halo B, the total mass is $1.42\text{--}5.62 M_\odot$ at 100–200 yr after PS1 formation, corresponding to the mass accretion rates $7.11 \times 10^{-3}\text{--}5.62 \times 10^{-2} M_\odot/\text{yr}$ and similarly evaluated temperatures 862–3416 K. The mass accretion rate for Halo A is lower than that for Halo B with a fixed metallicity because the gravitational potential of MHs, $\propto GM_{\text{vir}}/R_{\text{vir}}$, is shallower for Halo A ($1.2 \times 10^{11} \text{ erg g}^{-1}$) than for Halo B ($2.7 \times 10^{11} \text{ erg g}^{-1}$). Also, the gas in Halo A rotates more rapidly than Halo B and thus the centrifugal force effectively prevents the collapse and accretion. The rotation velocity of a cloud with mass M and density ρ is parametrized as

$$\beta = \frac{E_{\text{rot}}}{E_{\text{grav}}} = \frac{25}{12} \left(\frac{4\pi}{3} \right)^{1/3} \frac{J^2}{G\rho^{-1/3}M^{10/3}}. \quad (6)$$

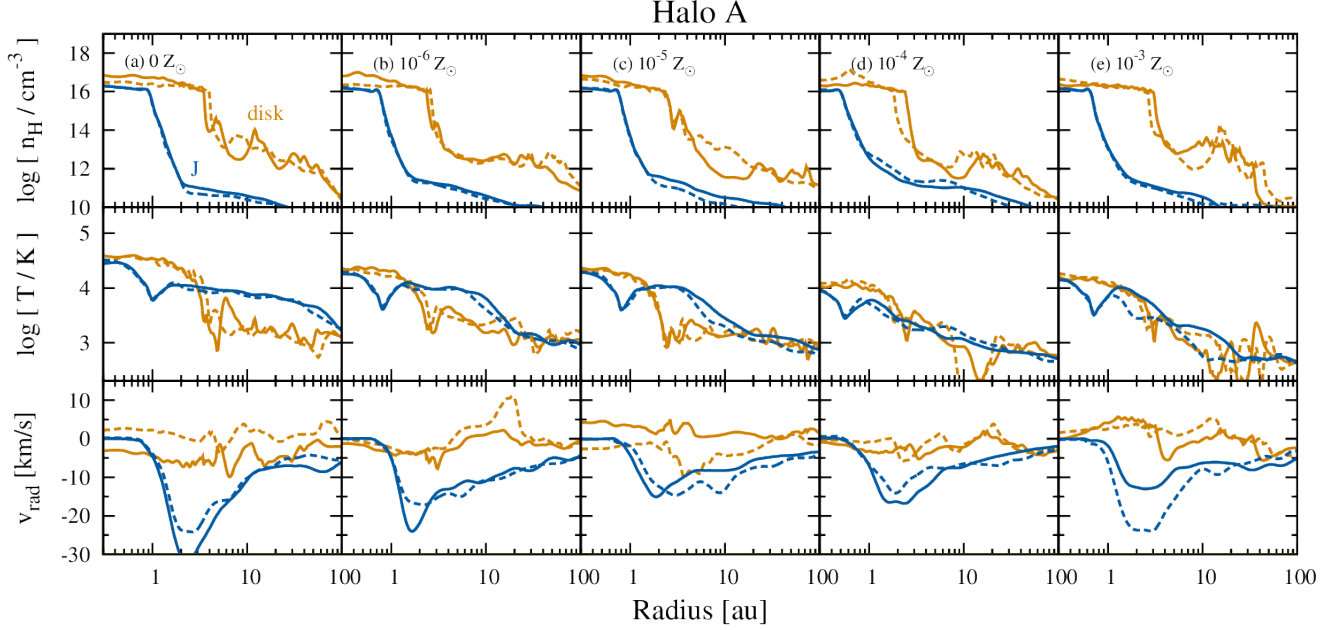


Figure 11. Density n_{H} (top panels), temperature T (middle panels), and radial velocity v_{rad} (bottom panels) as a function of distance from the center of mass of the most massive protostar. We plot the results for metallicities (a) $0 Z_{\odot}$, (b) $10^{-6} Z_{\odot}$, (c) $10^{-5} Z_{\odot}$, (d) $10^{-4} Z_{\odot}$, and (e) $10^{-3} Z_{\odot}$ for Halo A at the time when we terminate the simulations. The blue and orange curves show the results along the axes parallel and perpendicular (vertical axis in Fig. 5) to the angular momentum vector \mathbf{J} . The solid and dashed curves depict the opposite directions along these axes.

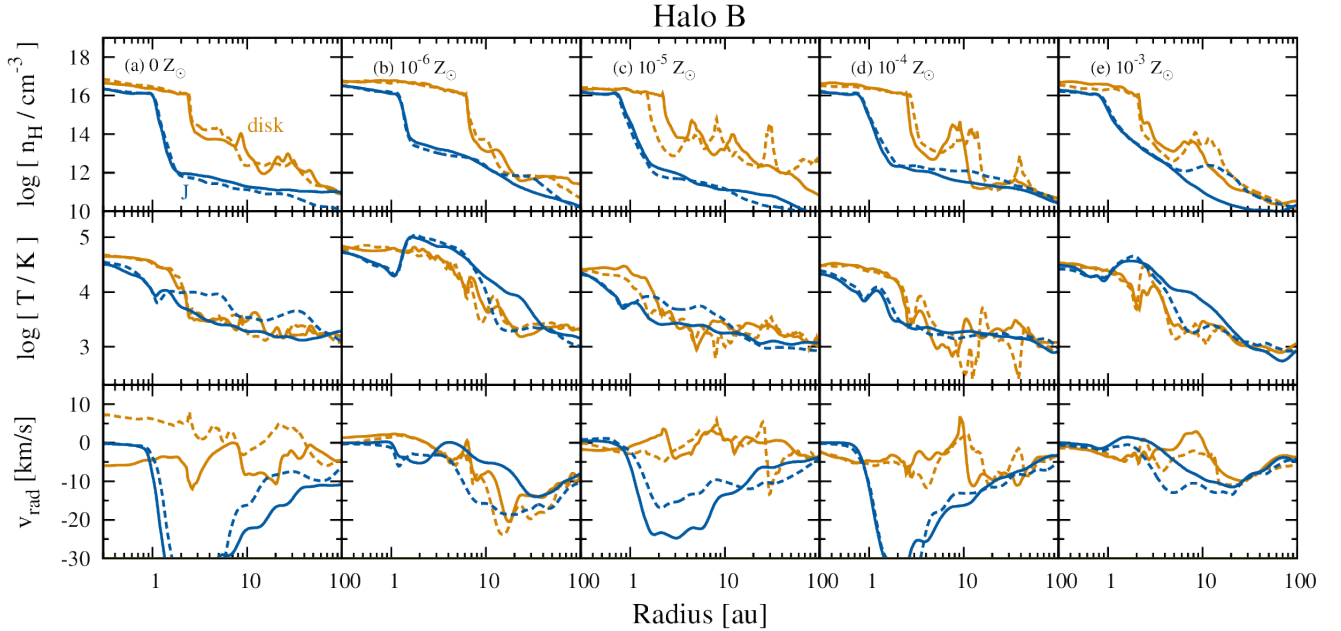


Figure 12. Same as Fig. 11 but for a minihalo Halo B.

In this equation, $E_{\text{rot}} \sim (\Omega R)^2 \sim (JR/I)^2$ is the rotational energy, where Ω , $I \sim MR^2 \sim M^{5/3} \rho^{-2/3}$, and $J = I\Omega$ are angular velocity, momentum of inertia, and total angular momentum, respectively, and $E_{\text{grav}} \sim GM/R$ is the gravitational energy. The parameter $\beta = 0.033$ of Halo A is larger than $\beta = 0.005$ of Halo B by a factor of seven.

Figs. 13 and 14 show the evolution of mass, accretion

rate, distance from the center of mass, and the angular momentum of each protostar for Halo A and B, respectively. Every protostar accretes the mass at the nearly constant rate around the average accretion rate shown in Table 2 (black dashed lines). All protostars are bound in the gravitational potential of the disc, and remain within $\lesssim 100$ au from the center of mass of the system. Several researchers reported

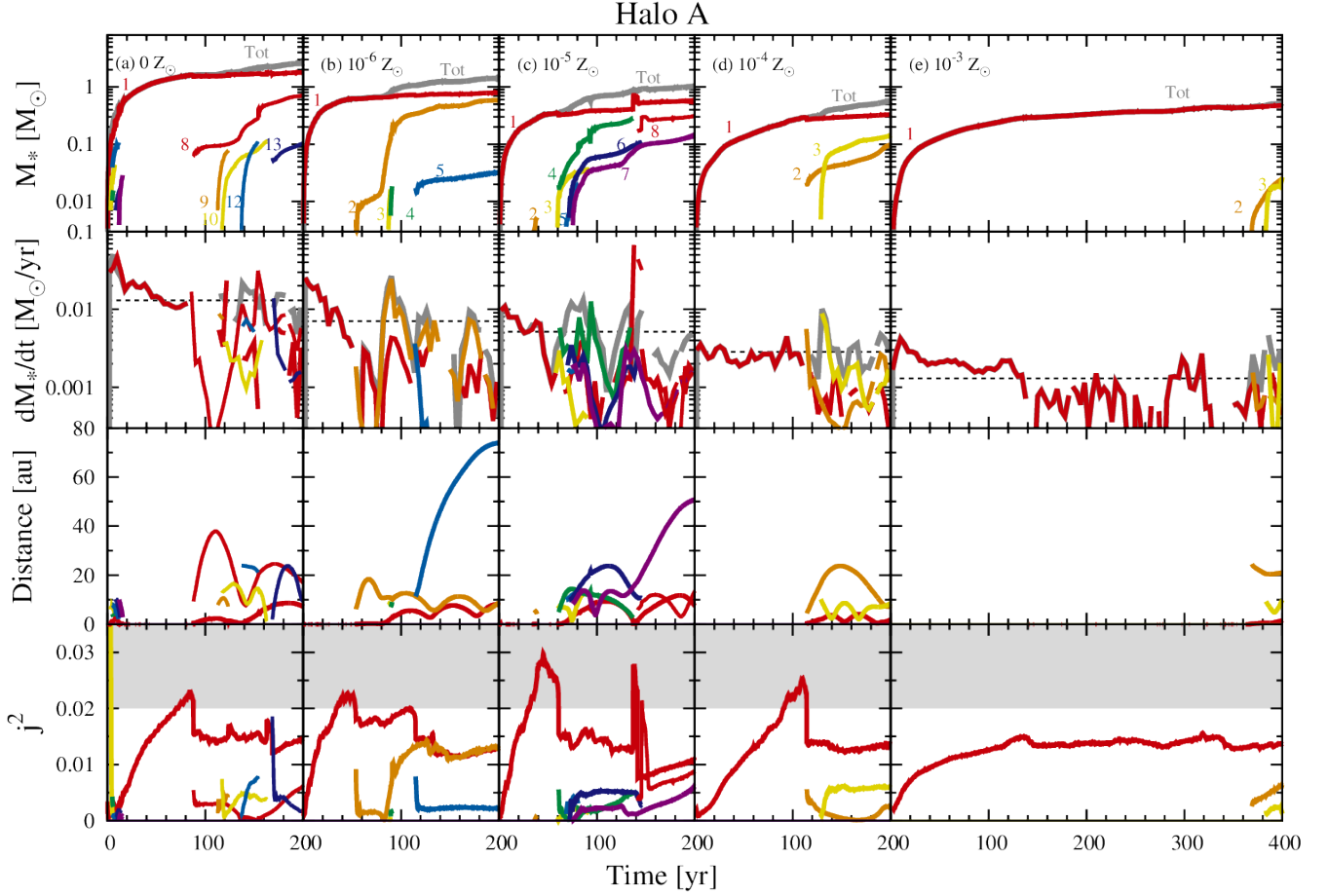


Figure 13. Time evolution of protostellar mass M_* , mass accretion rate \dot{M}_* , distance from the center of mass of the protostellar system, and the ratio of rotational energy to gravitational energy j^2 (Eq. 7). We plot the results with metallicities (a) 0, (b) $10^{-6} Z_\odot$, (c) $10^{-5} Z_\odot$, (d) $10^{-4} Z_\odot$, and (e) $10^{-3} Z_\odot$ for Halo A. The black dashed lines in the second row represent the average mass accretion rate. The grey shaded area represents the region of j^2 where break-up of a protostar occurs (see text).

that some protostars are ejected from a disc through N -body interactions (Clark et al. 2011; Greif et al. 2012). We do not see this slingshot effect in our simulations for a few 100 yrs of the disk evolution. The protostars also accrete angular momentum, and the parameter j^2

$$j^2 = \frac{J^2}{4\pi G \rho_*^{-1/3} M_*^{10/3}} \quad (7)$$

of protostars increases initially. The angular momentum of PS1 suddenly decreases when it is separated into two fragments by the centrifugal force (Appendix A). After the spiral arms develop in the discs, j^2 evolves nearly constantly due to the transport of angular momentum through the non-axisymmetric structure.

4 DISCUSSION

4.1 Final mass distribution

In principle, it is necessary to follow the disc and protostellar evolution for over $\sim 10^5$ yr until the protostars reach ZAMS, in order to determine the mass and the number of

stars forming in the system. Further fragmentation and gas accretion onto protostars will be halted by the radiative feedback when the primary protostars grow up to $7 M_\odot$ and start emitting ultraviolet photons (Hosokawa et al. 2016; Fukushima et al. 2020; Sugimura et al. 2020). If (a part of) protostars remain low-mass ($< 1 M_\odot$), they will be observed as extremely metal-poor binary systems or stellar clusters (Schlaufman et al. 2018; Arentsen et al. 2019). If they can grow up to $\sim 10 M_\odot$, the massive binaries or clusters can explain the origin of gravitational waves recently detected by LIGO/VIRGO because the mass-loss rate of metal-free and metal-poor stars is small in their main sequence, and most of their mass can contract into black holes (Abbott et al. 2016). To explicitly see the final fate of the protostellar system, we require another numerical strategy to extend the time for which we can follow the evolution of accretion discs, such as the sink particle technique. This work can supply additional models of the mergers and TDEs between sinks with sink particle algorithms.

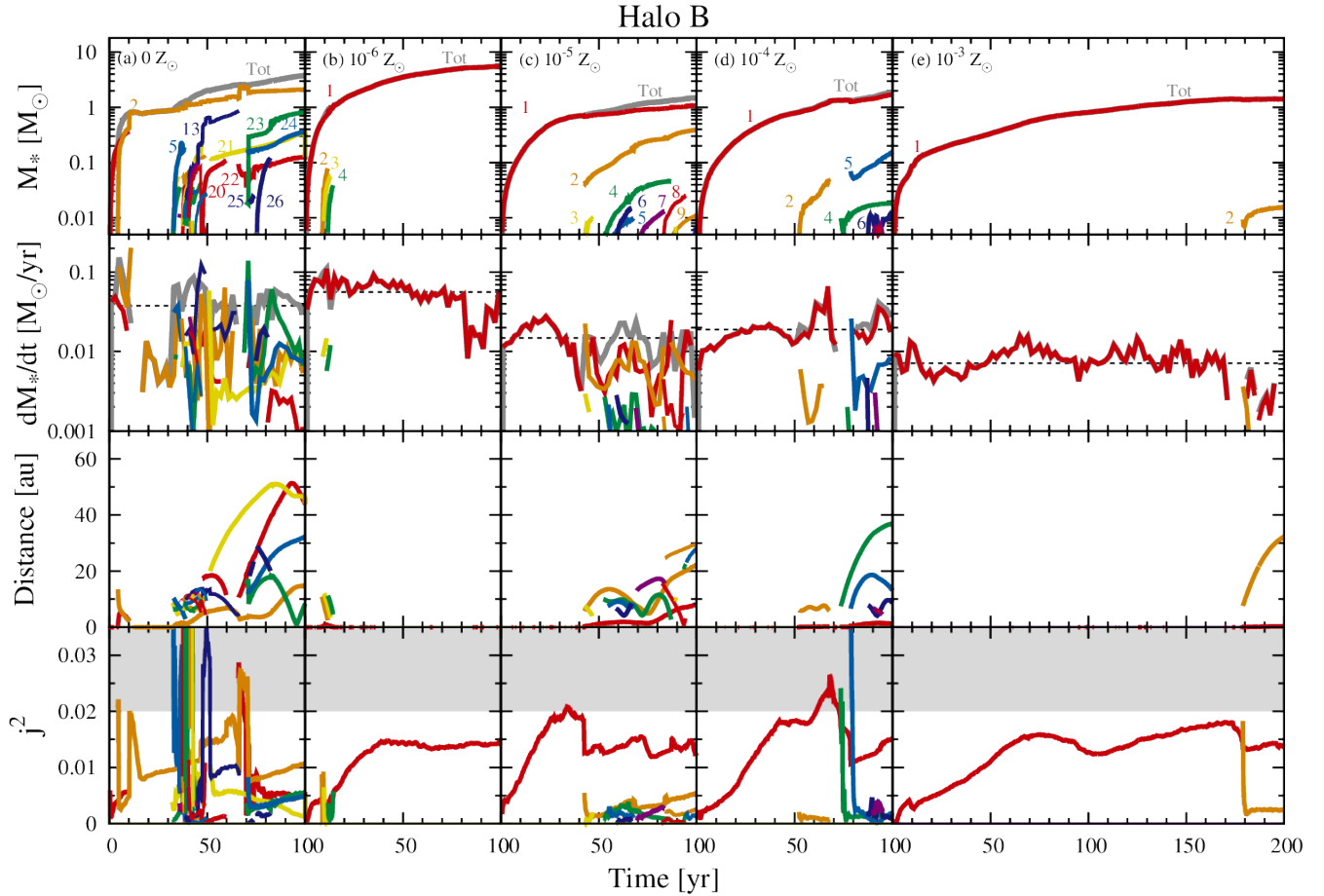


Figure 14. Same as Fig. 13 but for Halo B. The accretion rate is calculated every 2 yr.

4.2 Initial metal/dust models

The accretion rate decreases with the increasing dust cooling rate, which depends on the abundance and size distribution of dust grains. In this work we fix the initial metal and dust properties for a Pop III SN model with a progenitor mass $M_{\text{PopIII}} = 30 M_{\odot}$ and an ambient gas density $n_{\text{amb}} = 1 \text{ cm}^{-3}$. The dust cooling rate indeed depends on these parameters as studied by Chiaki et al. (2015). With $M_{\text{PopIII}} = 13 M_{\odot}$, growth of carbon grains also enhances the dust cooling rate because the elemental abundance of carbon is larger than oxygen. With increasing n_{amb} , depletion efficiency of metals onto grains decreases because the increasing rate of sputtering by reverse shocks. The critical metallicity above which dust cooling can operate increases by an order of magnitude for $n_{\text{amb}} = 10 \text{ cm}^{-3}$ than in the case without grain destruction. To statistically investigate the mass spectrum of Pop II stars, we need to consider the realistic ranges of M_{PopIII} and n_{amb} .

For the metal abundances of CEMP-no stars, we could discuss the condition for CF/DF in the analogy of this work. In our recent work (Chiaki et al. 2020), we followed the collapse of gas clouds with C-enhanced elemental abundance ratios. We employed “faint SN” models, where Fe-rich innermost layers are fallen back into a central SN remnant, and relatively C-enhanced gas is ejected (Umeda & Nomoto

2003). The enrichment from faint SNe is one of the scenarios that can explain the formation of CEMP-no stars. We found that the cloud core fragments due to rapid gas cooling from amorphous carbon grains for the lowest progenitor mass ($M_{\text{PopIII}} = 13 M_{\odot}$). Whereas, the clouds collapse stably even with efficient dust cooling because of H_2 formation heating for $M_{\text{PopIII}} = 50$ and $80 M_{\odot}$. Especially, for $M_{\text{PopIII}} = 50 M_{\odot}$, we found that spiral arms develop around the primary protostar. Since the Toomre Q parameter is below 0.6, the critical value for DF (Takahashi et al. 2016).

In this work, we have used a single Pop III SN model. Multiple Pop III and Pop II progenitors may contribute to metal enrichment of a halo. Hartwig et al. (2018) shows that C-normal stars with $[\text{Mg}/\text{C}] > -1$ are likely to form in clouds enriched by multiple progenitors, considering that only a part of Pop III stars explode as a faint SN and other SNe eject metals with similar abundance ratio. To compare with simulation results with the abundance pattern of observed EMP stars, we are required to consider multiply enriched gas clouds.

5 SUMMARY AND CONCLUSION

The mass distribution of metal-free and metal-poor stars is crucial to determine the strength of mechanical and chemical feedback in the early stage of galaxy formation. Numerical simulation is a powerful tool to study the mass evolution of multiple protostellar systems. In this paper, we have presented the results from a set of simulations that follow the protostellar evolution for several hundreds years. It has been conventionally postulated that the typical mass scale becomes smaller from Pop III to Pop II stars because of CF induced by additional cooling of dust thermal emission. We have shown that CF does not occur in most runs because the rapid gas heating associated with H_2 molecular formation. Although CF occurs in several runs, fragments are rapidly accreted onto the primary protostar. We have found that the dominant mode of fragmentation is DF regardless of metallicities. At most 26 protostars form through gas accretion or break-up, but most of them merge with each other or destroyed through TDEs. At the endpoint of our simulations, only several protostars remain in the systems. We have shown oligarchic evolution of the protostars where low-mass protostars orbiting around a massive star or around a massive binary.

We can know the mass distribution and multiplicity of finally forming stars after long-term evolution ($\sim 10^5$ yrs) of accretion discs. We have shown that the formation and destruction of protostars are on-going in the early accretion phase of a few 100 yrs. Gas accretion and fragmentation will be halted when the mass of the most massive protostar(s) exceeds $\sim 7 M_\odot$, and its radiative feedback is effective (Hosokawa et al. 2016). Whether low-mass or high-mass stars form depends on the strength and the timing of the radiative feedback. In future works, we will employ advanced numerical techniques, such as sink particles (see Fukushima et al. 2020), and will follow the long-term evolution of low-metallicity protostars.

ACKNOWLEDGMENTS

We thank T. Nozawa, who kindly give us the SN model, and H. Susa for fruitful discussions. GC is supported by Overseas Research Fellowships of the Japan Society for the Promotion of Science (JSPS) for Young Scientists. NY acknowledges support by SPPEXA through JST CREST JPMHCR1414. The numerical simulations and analyses in this work are carried out on XC40 in Yukawa Institute of Theoretical Physics (Kyoto University), and COMET in SDSC.

DATA AVAILABILITY

The versions of GRACKLE used in this work is available at <https://github.com/genchiaki/grackle/tree/metal-dust-radiation>. The data underlying this article will be shared on reasonable request to the authors.

REFERENCES

Abel, T., Bryan, G. L., & Norman, M. L. 2002, *Science*, 295, 93
Abbott B. P., et al., 2016, *PhRvL*, 116, 061102

Abbott, B. P., Abbott, R., Abbott, T. D., et al. 2017, *ApJ*, 848, L13
Aoki, W., Beers, T. C., Christlieb, N., et al. 2007, *ApJ*, 655, 492
Arentsen A., Starkenburg E., Shetrone M. D., Venn K. A., Depagne E., McConnachie A. W., 2019, *A&A*, 621, A108
Asplund, M., Grevesse, N., Sauval, A. J., & Scott, P. 2009, *ARA&A*, 47, 481
Barrow, K. S. S., Wise, J. H., Aykutaalp, A., et al. 2018, *MNRAS*, 474, 2617
Bianchi, S., & Schneider, R. 2007, *MNRAS*, 378, 973
Bovino, S., Grassi, T., Schleicher, D. R. G., & Banerjee, R. 2016, *ApJ*, 832, 154
Bromm, V., Coppi, P. S., & Larson, R. B. 1999, *ApJ*, 527, L5
Clark, P. C., Glover, S. C. O., Smith, R. J., et al. 2011, *Science*, 331, 1040
Chandrasekhar, S. 1962, *ApJ*, 136, 1048
Chandrasekhar, S. 1965, *ApJ*, 142, 890 111
Chiaki, G., Marassi, S., Nozawa, T., et al. 2015, *MNRAS*, 446, 2659
Chiaki, G., & Yoshida, N. 2015, *MNRAS*, 451, 3955
Chiaki, G., Yoshida, N., & Hirano, S. 2016, *MNRAS*, 463, 2781
Chiaki, G., Susa, H., & Hirano, S. 2018, *MNRAS*, 475, 4378
Chiaki, G., & Wise, J. H. 2019, *MNRAS*, 482, 3933
Chiaki G., Wise J. H., Marassi S., Schneider R., Limongi M., Chieffi A., 2020, *arXiv*, arXiv:2007.06657
Chon S., Hosokawa T., 2019, *MNRAS*, 488, 2658
Dopcke, G., Glover, S. C. O., Clark, P. C., & Klessen, R. S. 2011, *ApJ*, 729, L3
Eriguchi, Y., Hachisu, I., & Sugimoto, D. 1982, *Progress of Theoretical Physics*, 67, 1068
Fukushima H., Hosokawa T., Chiaki G., Omukai K., Yoshida N., Kuiper R., 2020, *MNRAS*, 497, 829
Grassi, T., Bovino, S., Haugbølle, T., & Schleicher, D. R. G. 2017, *MNRAS*, 466, 1259
Greif, T. H., Bromm, V., Clark, P. C., et al. 2012, *MNRAS*, 424, 399
Hartwig, T., Yoshida, N., Magg, M., et al. 2018, *MNRAS*, 478, 1795
Hirano, S., Hosokawa, T., Yoshida, N., et al. 2014, *ApJ*, 781, 60
Hirano, S., Hosokawa, T., Yoshida, N., Omukai, K., & Yorke, H. W. 2015, *MNRAS*, 448, 568
Hirano, S., & Bromm, V. 2017, *MNRAS*, 470, 898
Hosokawa, T., Hirano, S., Kuiper, R., et al. 2016, *ApJ*, 824, 119
Inoue, S., & Yoshida, N. 2018, *MNRAS*, 474, 3466
Inoue S., Yoshida N., 2020, *MNRAS*, 491, L24
Inutsuka, S.-I., & Miyama, S. M. 1997, *ApJ*, 480, 681
Ishigaki M. N., Tominaga N., Kobayashi C., Nomoto K., 2018, *ApJ*, 857, 46
Kitayama, T., Yoshida, N., Susa, H., & Umemura, M. 2004, *ApJ*, 613, 631
Komatsu, E., Smith, K. M., Dunkley, J., et al. 2011, *ApJS*, 192, 18
Larson, R. B. 1969, *MNRAS*, 145, 271
Liao W.-T., Turk M., 2019, *arXiv*, arXiv:1911.00610
Lyttleton, R. A. 1953, Cambridge: University Press, —c1953,
Machida, M. N., & Nakamura, T. 2015, *MNRAS*, 448, 1405
Nagasawa, M. 1987, *Progress of Theoretical Physics*, 77, 635
Nozawa, T., Kozasa, T., Umeda, H., Maeda, K., & Nomoto, K. 2003, *ApJ*, 598, 785
Nozawa, T., Kozasa, T., Habe, A., et al. 2007, *ApJ*, 666, 955
Omukai, K. 2000, *ApJ*, 534, 809
Penston, M. V. 1969, *MNRAS*, 144, 425
Pollack, J. B., Hollenbach, D., Beckwith, S., et al. 1994, *ApJ*, 421, 615
Rees M. J., 1988, *Natur*, 333, 523
Safranek-Shrader, C., Milosavljević, M., & Bromm, V. 2014, *MNRAS*, 440, L76

- Schlaufman, K. C., Thompson, I. B., & Casey, A. R. 2018, *ApJ*, 867, 98
- Schneider, R., Ferrara, A., Salvaterra, R., Omukai, K., & Bromm, V. 2003, *Nature*, 422, 869
- Smith, B. D., Wise, J. H., O’Shea, B. W., Norman, M. L., & Khochfar, S. 2015, *MNRAS*, 452, 2822
- Smith, B. D., Bryan, G. L., Glover, S. C. O., et al. 2017, *MNRAS*, 466, 2217
- Springel, V. 2005, *MNRAS*, 364, 1105
- Springel, V. 2010, *MNRAS*, 401, 791
- Stacy, A., Greif, T. H., & Bromm, V. 2012, *MNRAS*, 422, 290
- Sugimura, K., Mizuno, Y., Matsumoto, T., & Omukai, K. 2017, *MNRAS*, 469, 4022
- Sugimura K., Matsumoto T., Hosokawa T., Hirano S., Omukai K., 2020, *ApJL*, 892, L14
- Susa, H., Hasegawa, K., & Tominaga, N. 2014, *ApJ*, 792, 32
- Susa H., 2019, *ApJ*, 877, 99
- Takahashi, S. Z., Tsukamoto, Y., & Inutsuka, S. 2016, *MNRAS*, 458, 3597
- Tohline, J. E. 2002, *ARA&A*, 40, 349
- Truelove, J. K., Klein, R. I., McKee, C. F., et al. 1997, *ApJ*, 489, L179
- Truelove, J. K., Klein, R. I., McKee, C. F., et al. 1998, *ApJ*, 495, 821
- Tsuribe, T., & Omukai, K. 2006, *ApJ*, 642, L61
- Umeda, H., & Nomoto, K. 2002, *ApJ*, 565, 385
- Umeda, H., & Nomoto, K. 2003, *Nature*, 422, 871
- Whalen, D., Abel, T., & Norman, M. L. 2004, *ApJ*, 610, 14
- Whalen, D., van Veelen, B., O’Shea, B. W., & Norman, M. L. 2008, *ApJ*, 682, 49
- Wollenberg K. M. J., Glover S. C. O., Clark P. C., Klessen R. S., 2020, *MNRAS*, 494, 1871
- Yoshida, N., Omukai, K., Hernquist, L., & Abel, T. 2006, *ApJ*, 652, 6
- Yoshida N., Omukai K., Hernquist L., 2008, *Sci*, 321, 669

APPENDIX A: EVOLUTION OF PROTOSTELLAR SYSTEMS

In this work, we find that multiple protostellar systems form in the accretion discs. The protostars are created and destroyed through several processes. In this section, we in detail describe the mass evolution and the formation/destruction processes of each protostar.

A1 Formation of protostars

We find that protostars form through the following three processes: gravitational contraction (GC), break-up of a protostar (BU), and interaction of spiral arms (INT). Tables A1 and A2 show the formation time t_{form} and the formation path of each protostar in our simulations for Halo A and B, respectively. We discuss the physical mechanism for each process in detail.

A1.1 Gravitational contraction

In all runs, the primary protostar, PS1, forms and grows through gas accretion mostly through filaments. PS1 continues to be the most massive protostar until the simulation is terminated (see red curves in Figs. 13 and 14) in all runs but for HBZ0 where PS2 eventually becomes most massive one. The secondary protostars also form through gas accretion for very low metallicities $< 10^{-6} Z_{\odot}$. H_2 cooling

induces the deformation of cloud cores, and dense filaments form, where the secondary protostars form due to the gravitational instabilities within $t_* \sim 15$ yr. For example, Fig. A1 shows the formation of protostars through the gravitational contraction for HBZ-6. At $t_* = 8.3, 9.5$, and 11.5 yr, PS2, PS3, and PS4 form at distances 10.9, 12.0, and 11.2 au from PS1, respectively. Linear analyses show that the most unstable wave number of perturbations on an isothermal filament is $\lambda_{\text{max}} = 2\pi H$, where $H = (2c_s^2/\pi G\rho)^{1/2}$ is the scale height, or an effective radius of the filament (Nagasawa 1987; Inutsuka & Miyama 1997). We can estimate the length-scale where fragmentation occurs to be $\lambda_{\text{max}} = 16.2$ au for $n_H = 10^{14} \text{ cm}^{-3}$ and $T = 1000$ K. The initial separation between the secondary protostars and PS1 is comparable to this analytic estimate. This is also consistent with the findings of our previous study (C16).

A1.2 Break-up

Another interesting case is found for HAZ-4. After PS1 sufficiently accretes mass and angular momentum, it breaks up into two protostars when the centrifugal force overcomes the gravitational force (see Fig. A2). Until we terminate the simulation, the protostar forming through break-up survive because its initial orbital angular velocity is comparable to the escape velocity of the primary protostar. The protostars formed in this way become eventually as the second most massive protostar in eight out of ten runs (all but for HAZ-3 and HBZ-6).

Fig. A2 shows the process of break-up for HAZ-4. Since PS1 forms in the filament, it has a bar-like shape from the beginning. After PS1 acquires sufficient angular momentum, perturbations of the third or higher-order grow and PS1 is deformed to have “dumb-bell-shape”.⁵ The dumb-bell structure is deformed further and the protostar is eventually divided into two separate ones. In the classical theory of “fission”, an object break-up into an equal-mass binary (Lyttleton 1953). In our run HAZ-4, only 7% of mass is taken apart from the main body, which thus should be more appropriately characterized as “mass-shedding” suggested by Eriguchi et al. (1982).

Protostars forming through the break-up show interesting accretion histories, as shown in Figs 13 and 14 (see the orange curve in Fig. 13b as a notable example). Within ~ 10 yr after its formation, the secondary protostar accretes gas rapidly because it is still in a dense spiral arm. Then the secondary protostar is ejected to a few tens au away from the center, where the gas density is as low as 10^{14} cm^{-3} , and thus the accretion rate is low. Since the initial ejection velocity is less than the escape velocity of the accretion disc, the protostar falls back onto the dense region and orbits around PS1. The accretion rate increases again up to the value comparable to that of PS1.

The criterion for the break-up can be expressed by the critical angular momentum. As in Eriguchi et al. (1982), we

⁵ More strictly, it is a Jacobi ellipsoid that can have a “dumb-bell-shape” (Eriguchi et al. 1982). Protostars in our simulations are more oblate with aspect ratios < 0.25 , below the Jacobi sequence. Further detailed modelling is needed to investigate a criterion for the break-up of such oblate objects (Tohline 2002).

Table A1. Properties of protostars for Halo A

| Z [Z_\odot] | i | t_{form} [yr] | form | parent | t_{dest} [yr] | dest. | j | b [au] | a_j [au] | m_j/m_i | r_{tid} [au] | t_{life} [yr] | M_* [M_\odot] |
|----------------------|-----|---------------------------|------|--------|---------------------------|-------|-----|-------------|---------------|-----------|--------------------------|---------------------------|------------------------|
| 10^{-3} | 1 | 2.7 | GC | — | — | — | — | — | — | — | — | — | 0.471 |
| | 2 | 368.7 | INT | — | — | — | — | — | — | — | — | — | 0.025 |
| | 3 | 383.3 | INT | — | — | — | — | — | — | — | — | — | 0.026 |
| 10^{-4} | 1 | 1.5 | GC | — | — | — | — | — | — | — | — | — | 0.328 |
| | 2 | 114.3 | BU | 1 | — | — | — | — | — | — | — | — | 0.097 |
| | 3 | 128.7 | INT | — | — | — | — | — | — | — | — | — | 0.142 |
| 10^{-5} | 1 | 0.9 | GC | — | — | — | — | — | — | — | — | — | 0.584 |
| | 2 | 35.9 | INT | — | 39.1 | MER | 1 | 3.72 | 4.22 | 53.07 | 15.87 | 3.2 | (0.005) |
| | 3 | 59.7 | INT | — | 92.3 | MER | 4 | 0.13 | 1.05 | 3.39 | 1.57 | 32.6 | (0.037) |
| | 4 | 60.9 | BU | 1 | 137.1 | TDE | 1 | 3.82 | 2.03 | 1.44 | 2.30 | 76.2 | (0.283) |
| | 5 | 68.7 | INT | — | 80.9 | TDE | 4 | 1.16 | 0.74 | 3.73 | 1.15 | 12.2 | (0.020) |
| | 6 | 71.7 | INT | — | 145.7 | TDE | 8 | 3.03 | 1.51 | 1.63 | 1.78 | 74.0 | (0.110) |
| | 7 | 75.3 | INT | — | — | — | — | — | — | — | — | — | 0.140 |
| | 8 | 141.5 | BU | 1 | — | — | — | — | — | — | — | — | 0.309 |
| 10^{-6} | 1 | 0.3 | GC | — | — | — | — | — | — | — | — | — | 0.795 |
| | 2 | 53.9 | BU | 1 | — | — | — | — | — | — | — | — | 0.580 |
| | 3 | 87.1 | INT | — | 89.5 | MER | 2 | 1.00 | 1.19 | 7.57 | 2.33 | 2.4 | (0.016) |
| | 4 | 89.3 | INT | — | 90.9 | TDE | 2 | 1.59 | 1.48 | 8.29 | 3.00 | 1.6 | (0.018) |
| | 5 | 114.9 | BU | 1 | — | — | — | — | — | — | — | — | 0.032 |
| 0 | 1 | 0.3 | GC | — | — | — | — | — | — | — | — | — | 1.782 |
| | 2 | 3.1 | GC | — | 3.3 | MER | 1 | 0.00 | 4.13 | 17.87 | 10.79 | 0.2 | (0.005) |
| | 3 | 3.3 | GC | — | 7.7 | MER | 1 | 0.61 | 1.27 | 4.51 | 2.10 | 4.4 | (0.044) |
| | 4 | 4.9 | GC | — | 6.3 | MER | 1 | 0.32 | 1.11 | 9.66 | 2.37 | 1.4 | (0.016) |
| | 5 | 4.9 | GC | — | 11.7 | MER | 1 | 0.87 | 1.39 | 2.96 | 1.99 | 6.8 | (0.107) |
| | 6 | 8.5 | GC | — | 13.5 | MER | 1 | 1.02 | 2.63 | 26.32 | 7.83 | 5.0 | (0.017) |
| | 7 | 11.9 | GC | — | 15.7 | MER | 1 | 1.36 | 2.14 | 17.50 | 5.55 | 3.8 | (0.029) |
| | 8 | 87.9 | BU | 1 | — | — | — | — | — | — | — | — | 0.712 |
| | 9 | 112.7 | INT | — | 123.5 | DIS | — | 5.26 | 4.01 | 20.30 | 10.93 | 10.8 | (0.078) |
| | 10 | 117.1 | INT | — | 163.1 | TDE | 1 | 5.64 | 4.16 | 15.11 | 10.29 | 46.0 | (0.110) |
| | 11 | 123.7 | GC | — | 123.9 | TDE | 1 | 0.49 | 4.11 | 20.36 | 11.23 | 0.2 | (0.077) |
| | 12 | 137.1 | INT | — | 154.1 | MER | 8 | 0.22 | 1.05 | 2.56 | 1.44 | 17.0 | (0.111) |
| | 13 | 168.5 | BU | 1 | — | — | — | — | — | — | — | — | 0.103 |

Note — (1) Metallicity Z . (2) ID of a protostar i . (3) Formation time t_{form} of protostars. (4) Formation paths of each protostar: gravitational contraction (GC), break-up of a parent protostar (BU), and interaction of spiral arms (SAI). (5) ID of the parent protostar which breaks up. (6) Destruction time t_{dest} of protostars. (7) Destruction mechanism: merger (MER), tidal disruption event (TDE), and dissolution to the ambient gas (DIS). (8) ID of counterpart j with which the protostar i interacts. (9-12) Impact parameter b , radius of major-axis r_j , mass ratio m_j/m_i , and tidal radius r_{tid} of the impactor j . (13) Life time t_{life} of the protostar. (14) protostellar mass M_* when it is destroyed with parentheses or when the simulation is terminated at $t_{*,\text{fin}}$ without parentheses.

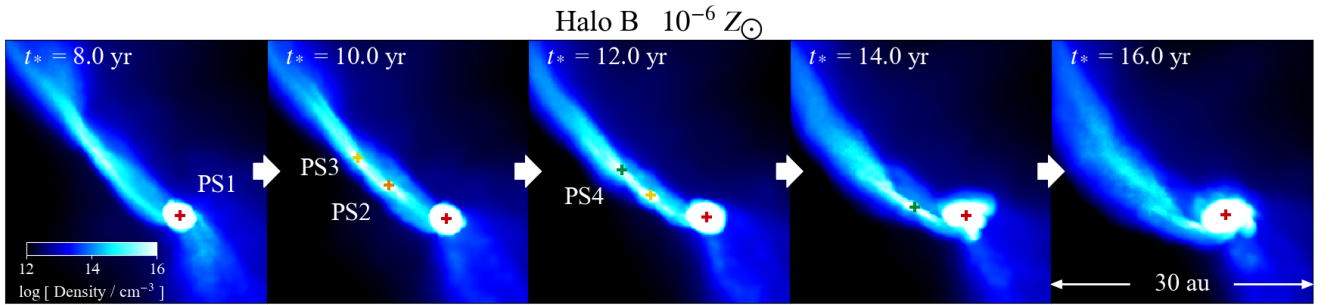


Figure A1. Projection of density in the accretion disc for HBZ6 from $t_* = 8$ to 16 yr, where the gravitational contraction of the dense filament drives protostar formation.

Table A2. Properties of protostars for Halo B

| Z [Z_{\odot}] | i | t_{form} [yr] | form | parent | t_{dest} [yr] | dest. | j | b [au] | a_j [au] | m_j/m_i | r_{tid} [au] | t_{life} [yr] | M_* [M_{\odot}] |
|------------------------|-----|---------------------------|------|--------|---------------------------|-------|-----|-------------|---------------|-----------|--------------------------|---------------------------|--------------------------|
| 10^{-3} | 1 | 0.7 | GC | — | — | — | — | — | — | — | — | — | 1.407 |
| | 2 | 178.9 | BU | 1 | — | — | — | — | — | — | — | — | 0.015 |
| 10^{-4} | 1 | 1.3 | GC | — | — | — | — | — | — | — | — | — | 1.693 |
| | 2 | 52.3 | INT | — | 67.9 | MER | 1 | 5.96 | 6.46 | 28.11 | 19.63 | 15.6 | (0.044) |
| | 3 | 69.9 | GC | — | 70.1 | DIS | — | 0.00 | 5.20 | 280.10 | 34.00 | 0.2 | (0.005) |
| | 4 | 73.5 | BU | 1 | — | — | — | — | — | — | — | — | 0.018 |
| | 5 | 78.5 | BU | 1 | — | — | — | — | — | — | — | — | 0.156 |
| | 6 | 87.5 | INT | — | — | — | — | — | — | — | — | — | 0.012 |
| | 7 | 90.1 | INT | — | 95.1 | TDE | 1 | 5.83 | 4.21 | 328.25 | 29.06 | 5.0 | (0.005) |
| | 8 | 92.5 | INT | — | 93.5 | TDE | 1 | 5.85 | 3.74 | 287.93 | 24.68 | 1.0 | (0.005) |
| | 9 | 94.5 | BU | 1 | 94.7 | MER | 1 | 0.84 | 4.11 | 420.29 | 30.81 | 0.2 | (0.004) |
| 10^{-5} | 1 | 0.5 | GC | — | — | — | — | — | — | — | — | — | 1.076 |
| | 2 | 42.5 | BU | 1 | — | — | — | — | — | — | — | — | 0.393 |
| | 3 | 42.7 | INT | — | 46.9 | TDE | 1 | 3.11 | 2.52 | 76.74 | 10.71 | 4.2 | (0.009) |
| | 4 | 52.3 | INT | — | 87.1 | TDE | 1 | 3.15 | 3.07 | 21.49 | 8.54 | 34.8 | (0.045) |
| | 5 | 54.5 | INT | — | 67.9 | TDE | 2 | 1.38 | 1.25 | 16.93 | 3.20 | 13.4 | (0.010) |
| | 6 | 58.7 | INT | — | 66.7 | TDE | 2 | 1.35 | 1.13 | 10.96 | 2.52 | 8.0 | (0.015) |
| | 7 | 69.3 | INT | — | 83.7 | TDE | 2 | 1.57 | 1.25 | 20.51 | 3.41 | 14.4 | (0.013) |
| | 8 | 82.3 | INT | — | 94.5 | MER | 1 | 1.64 | 3.78 | 41.05 | 13.03 | 12.2 | (0.025) |
| | 9 | 83.9 | INT | — | — | — | — | — | — | — | — | — | 0.011 |
| | 10 | 89.1 | BU | 1 | 89.7 | DIS | — | 4.44 | 3.14 | 317.30 | 21.45 | 0.6 | (0.003) |
| | 11 | 93.3 | GC | — | 94.5 | DIS | — | 11.55 | 3.78 | 330.92 | 26.12 | 1.2 | (0.003) |
| | 12 | 94.7 | GC | — | — | — | — | — | — | — | — | — | 0.005 |
| | 13 | 99.1 | BU | 1 | 99.5 | DIS | — | 4.46 | 3.59 | 196.66 | 20.86 | 0.4 | (0.005) |
| 10^{-6} | 1 | 0.5 | GC | — | — | — | — | — | — | — | — | — | 5.615 |
| | 2 | 8.3 | GC | — | 11.7 | MER | 1 | 1.17 | 1.99 | 9.60 | 4.23 | 3.4 | (0.078) |
| | 3 | 9.5 | GC | — | 13.1 | MER | 1 | 1.80 | 2.55 | 15.96 | 6.43 | 3.6 | (0.057) |
| | 4 | 11.5 | GC | — | 14.5 | TDE | 1 | 2.62 | 2.24 | 25.98 | 6.65 | 3.0 | (0.039) |
| 0 | 1 | 0.3 | GC | — | 10.3 | TDE | 2 | 3.70 | 2.06 | 1.15 | 2.15 | 10.0 | (0.365) |
| | 2 | 4.3 | INT | — | — | — | — | — | — | — | — | — | 2.113 |
| | 3 | 32.1 | INT | — | 35.5 | TDE | 2 | 3.92 | 2.61 | 16.01 | 6.57 | 3.4 | (0.056) |
| | 4 | 32.5 | INT | — | 36.3 | MER | 7 | 0.76 | 0.77 | 0.32 | 1.25 | 3.8 | (0.036) |
| | 5 | 32.7 | INT | — | 39.1 | TDE | 2 | 3.42 | 2.97 | 5.89 | 5.36 | 6.4 | (0.167) |
| | 6 | 33.1 | BU | 5 | 33.3 | MER | 5 | 1.06 | 2.18 | 3.29 | 3.25 | 0.2 | (0.005) |
| | 7 | 35.9 | INT | — | 36.3 | MER | 4 | 0.76 | 0.86 | 3.08 | 1.25 | 0.4 | (0.012) |
| | 8 | 37.3 | BU | 5 | 40.9 | MER | 13 | 0.66 | 0.67 | 1.49 | 0.77 | 3.6 | (0.024) |
| | 9 | 37.5 | INT | — | 49.3 | TDE | 13 | 3.87 | 3.73 | 3.88 | 5.86 | 11.8 | (0.133) |
| | 10 | 37.5 | INT | — | 47.7 | TDE | 13 | 4.31 | 2.16 | 1.16 | 2.27 | 10.2 | (0.203) |
| | 11 | 38.1 | BU | 2 | 47.1 | MER | 10 | 2.05 | 2.51 | 3.24 | 3.71 | 9.0 | (0.045) |
| | 12 | 38.3 | INT | — | 45.5 | TDE | 9 | 1.88 | 0.90 | 2.77 | 1.26 | 7.2 | (0.031) |
| | 13 | 38.9 | INT | — | 66.5 | TDE | 2 | 5.71 | 2.80 | 1.71 | 3.35 | 27.6 | (0.855) |
| | 14 | 40.5 | INT | — | 45.3 | TDE | 13 | 1.24 | 1.05 | 0.98 | 1.03 | 4.8 | (0.097) |
| | 15 | 40.5 | INT | — | 49.3 | MER | 2 | 3.22 | 4.10 | 305.09 | 27.59 | 8.8 | (0.004) |
| | 16 | 41.1 | BU | 2 | 41.7 | TDE | 15 | 5.21 | 1.26 | 7.53 | 2.47 | 0.6 | (0.003) |
| | 17 | 42.1 | INT | — | 43.3 | TDE | 15 | 5.49 | 0.90 | 12.91 | 2.12 | 1.2 | (0.004) |
| | 18 | 42.7 | BU | 11 | 43.7 | TDE | 10 | 1.92 | 1.50 | 3.48 | 2.28 | 1.0 | (0.023) |
| | 19 | 43.9 | INT | — | 49.9 | MER | 2 | 3.48 | 4.10 | 48.15 | 14.91 | 6.0 | (0.027) |
| | 20 | 47.5 | INT | — | 59.9 | TDE | 2 | 4.84 | 4.33 | 12.93 | 10.16 | 12.4 | (0.109) |
| | 21 | 51.5 | INT | — | — | — | — | — | — | — | — | — | 0.352 |
| | 22 | 65.9 | INT | — | — | — | — | — | — | — | — | — | 0.126 |
| | 23 | 69.9 | INT | — | — | — | — | — | — | — | — | — | 0.815 |
| | 24 | 70.7 | BU | 2 | — | — | — | — | — | — | — | — | 0.365 |
| | 25 | 71.5 | INT | — | 73.9 | TDE | 22 | 1.50 | 0.94 | 2.54 | 1.28 | 2.4 | (0.022) |
| | 26 | 75.3 | INT | — | 82.5 | MER | 23 | 1.02 | 1.56 | 3.44 | 2.36 | 7.2 | (0.121) |

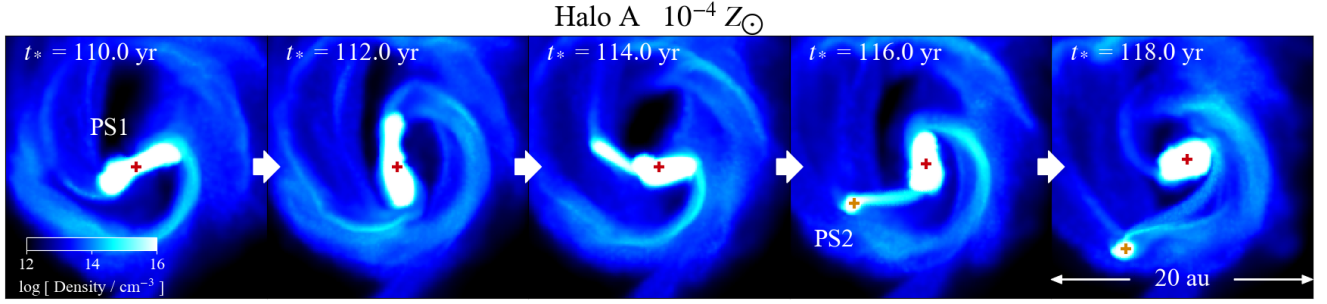


Figure A2. Projection of density in the accretion disc for HAZ4 from $t_* = 110$ to 118 yr, where the break-up of a rapidly rotating protostar PS1 generates a protostar PS2.

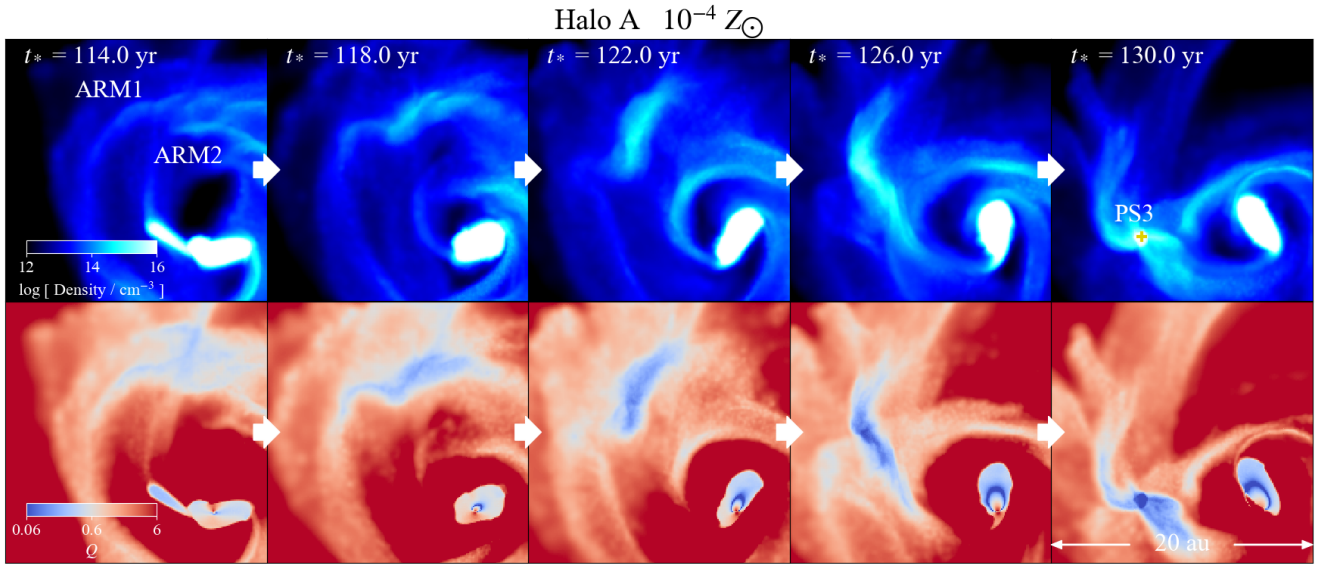


Figure A3. Projections of density (top panels) and Toomre Q parameter (bottom panels) in the accretion disc for HAZ-4 from $t_* = 114$ to 130 yr, where the interaction between two spiral arms ARM1 and ARM2 drives formation of a protostar PS3.

introduce a dimensionless parameter j^2 (Eq. 7), which is the same order as β (Eq. 6). The lower panels of Figs. 13 and 14 show the evolution of j^2 . Until the break-up occurs, j^2 of PS1 constantly increases along with mass accretion. After j^2 exceeds a critical value $j_{\text{cr}}^2 = 0.02$, the break-up occurs, and then j^2 decreases below j_{cr}^2 . We indicate the region with $j^2 > j_{\text{cr}}^2$ with shades in Figs. 13 and 14. In our simulations, j^2 of PS1 reaches around j_{cr}^2 in all cases except for HAZ-3 and HBZ-6, where no protostars form through the break-up.

We estimate the lower-limit of the initial β of a cloud with a density $n_{\text{H,cl}}$, above which the break-up of protostars occur after the gas density increases up to a density $n_{\text{H,*}}$. Assuming that the angular momentum will be conserved in the region that contains the mass of M_* in the cloud, we derive the critical value of β as

$$\beta_{\text{cr}} = 4 \times 10^{-5} \left(\frac{n_{\text{H,cl}}}{10^3 \text{ cm}^{-3}} \right)^{1/3} \left(\frac{n_{\text{H,*}}}{10^{16} \text{ cm}^{-3}} \right)^{-1/3} \left(\frac{j_{\text{cr}}^2}{0.02} \right). \quad (\text{A1})$$

The range of β of MHs are 0.1–1 (Hirano et al. 2014), which suggests that protostars forming in MHs can generally frag-

ment through the break-up. We note that, in actual protostellar discs, angular momentum is transported through non-axisymmetric structures, and then larger β_{cr} would be necessary for break-up so that the protostar obtain sufficient rotational energy larger than j_{cr}^2 .

A1.3 Interaction of spiral arms

There is yet another mode of protostar formation through the interaction of spiral arms around PS1. Since a spiral arm has larger rotational velocity in the inner region, it collide with spiral arm(s) in outer region. The gas at the colliding interface between two spiral arms is compressed and becomes gravitationally unstable. Fig. A3 shows that spiral arms ARM1 and ARM2 collide with each other and produce a dense blob. The blob eventually becomes self-gravitating, and a protostar PS3 forms at $t_* = 130$ yr for HAZ-4. Following Takahashi et al. (2016) and Inoue & Yoshida (2018), we calculate the Toomre Q parameter $Q = c_s \kappa / \pi G \Sigma$, where κ is the epicyclic frequency here estimated as 2Ω and Σ is the

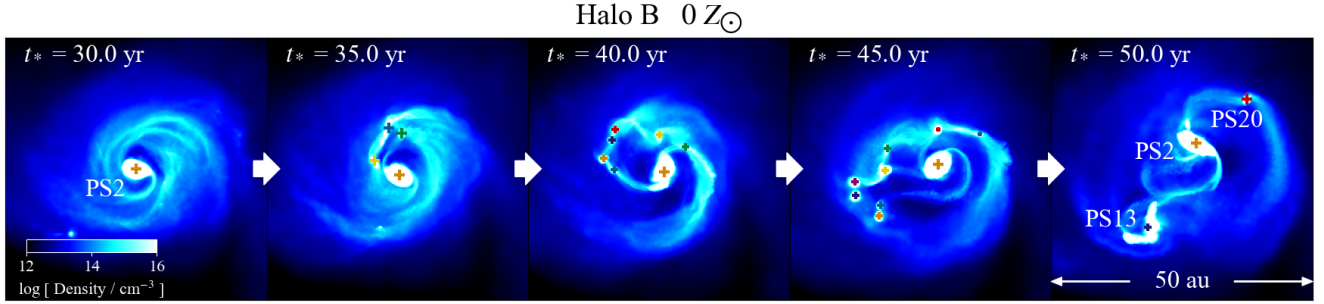


Figure A4. Projection of density in the accretion disc for HAZO from $t_* = 30$ to 50 yr, where > 20 protostars rapidly forms.

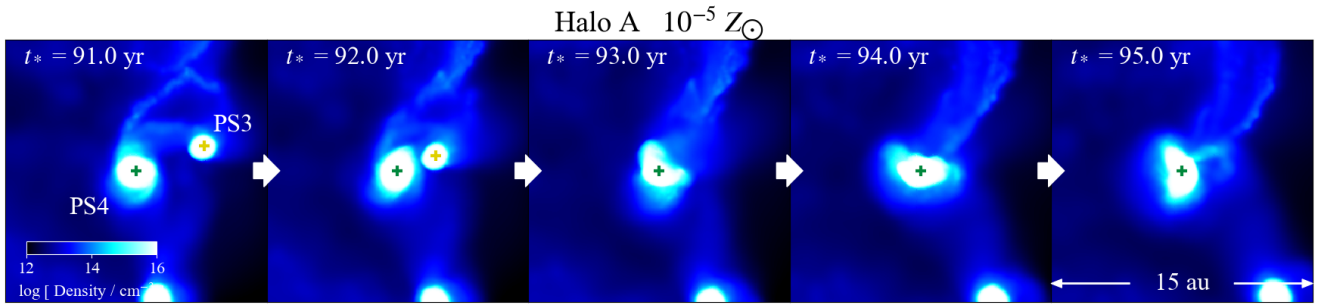


Figure A5. Projection of density in the accretion disc for HBZ-5 from $t_* = 91$ to 95 yr, where merger of protostars occurs.

gas surface density. We integrate c_s , Ω , and Σ in the direction of angular momentum vector of the inner disc defined as the region with densities $n_H > 10^{14} \text{ cm}^{-3}$. Takahashi et al. (2016) suggest that fragmentation along spiral arms in an accretion disc occurs with $Q < 0.6$. The lower panels of Fig. A3 show that Q is marginally small, $Q \simeq 0.6$, on ARM1 and ARM2. After the two arms collide, Σ becomes larger by an order of magnitude. Then, the locally estimated Q is below 0.6; the dense region grows to a separate protostar PS3. DF through interaction of spiral arms are studied by Inoue & Yoshida (2020). They perform detailed analysis of time evolution of spiral arms using an analytic model and direct simulations, to define the conditions for fragmentation.

A2 Destruction of protostars

Although at most 26 protostars form in an accretion disc in the first few hundred years, only 2–5 protostars survive after the destruction processes of protostars. Fig. A4 shows the result of our run HBZ0; more than 20 protostars form within 50 yr in the accretion disc with a high accretion rate ($\simeq 0.04 M_\odot/\text{yr}$ at $t_* \simeq 40$ yr). Most of the protostars merge with the massive protostars PS2, PS13, and PS20, and only the three massive protostars survive at $t_* = 50$ yr. There are a few characteristic destruction processes: dissolution of protostars into ISM (DIS), mergers (MER), and TDEs. Tables A1 and A2 show the time t_{dest} and path of destruction. We discuss each process in detail.

A2.1 Dissolution into ISM

Some protostars are dissolved into ISM. They are born with masses around the minimum mass $M_* = 0.003 M_\odot$ above which we define a clump as a protostar. These protostars lose their mass because they are inefficiently self-gravitated.

A2.2 Mergers

Other protostars are destroyed through the interaction with another protostar. The interaction can be divided into two categories: MER and TDE. We define the criterion of MER and TDE by comparing the impact parameter of an approaching protostar and the radius of a target protostar. For a protostar PS_i approaching a protostar PS_j , we calculate the impact parameter b from the position and velocity of PS_i relative to PS_j from the snapshot taken just before the destruction. Then, we calculate the radius (major axis) a_j of PS_j by approximating its shape as an ellipsoid. We define the interaction between PS_i and PS_j as MER if $b < a_j$, and as TDE otherwise. The criterion is different from the conventional one as we discuss in the next section. The 9th and 10th columns of Tables A1 and A2 show mass the impact parameter b and radius a_j just before MER or TDE. Fig. A5 shows that a protostar PS3 merges with PS4 at $t_* = 92.3$ yr for HAZ-5. PS3 approaches PS4 with impact parameter of $b = 0.13$ au. It is smaller than the radius of PS4 $a_4 = 1.05$ au. A near head-on collision occurs and PS3 merges without a TDE.

Most protostars form in dense spiral arms around the most massive protostar. The protostars lose their angu-

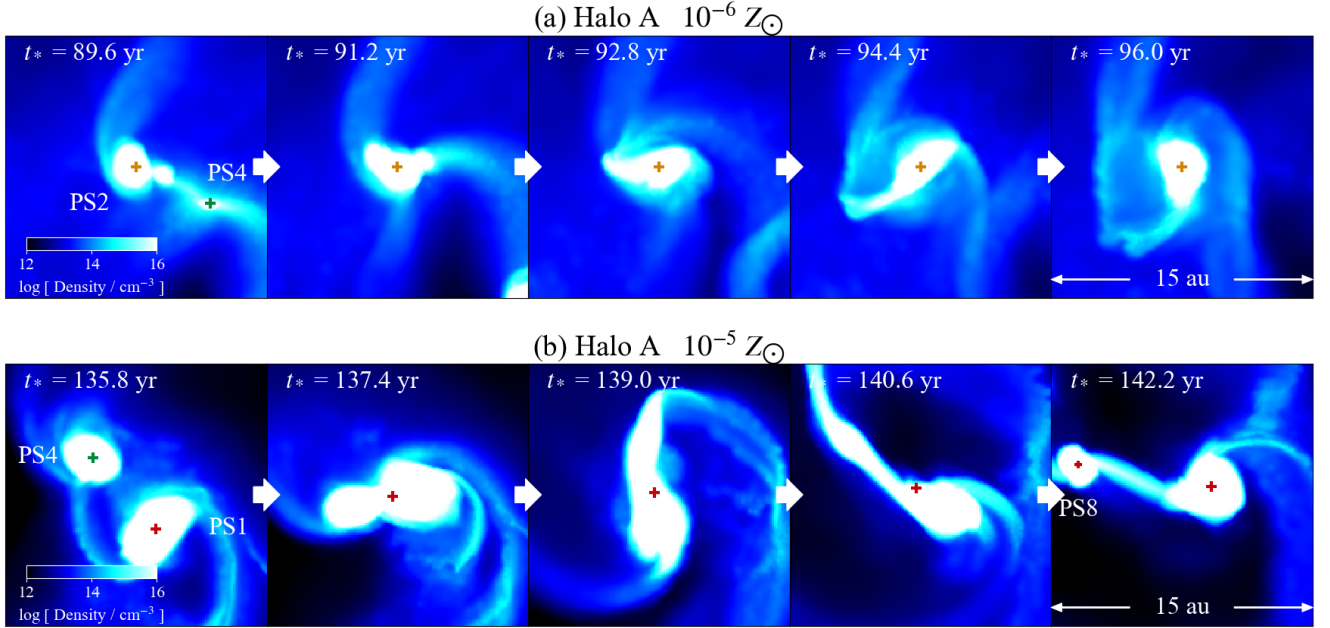


Figure A6. Projection of density in the accretion discs for (a) HAZ-6 and (b) HAZ-5, where tidal disruption events (TDEs) occur.

lar momentum from the non-axisymmetric structure. Then, they migrate toward PS1 in the manner of Type I migration as reported in Greif et al. (2012) and Hosokawa et al. (2016). The migration time scale is comparable to the free-fall time $t_{\text{ff}} = 4.5$ yr in the region with density $n_{\text{H}} = 10^{14} \text{ cm}^{-3}$. The life time of the protostars which merge with PS1 in our simulations is found to be typically ~ 1 – 10 yr (Tables A1 and A2). Since this is comparable to the free-fall timescale, we conclude that the protostars undergo Type I migration (also see Chon & Hosokawa 2019; Liao & Turk 2019) and merge with the central protostar.

A2.3 Tidal disruption events

Some protostars are destroyed through tidal disruption events (TDEs). Fig. A6a shows a TDE of PS4 with PS2 at $t_* = 90.0$ yr for HAZ-6. The impact parameter between them is $b = 1.59$ au. It is larger than the radius of PS2 $a_2 = 0.48$ au, but smaller than the tidal radius $r_{\text{tid}} = 3.00$ au. During the collision, PS4 is strongly deformed by the tidal force of PS2, and dense arm-like structures form around PS2. The whole elongated structure is eventually accreted onto PS4. We also find a case where another protostar forms from the dense, deformed structure after TDEs. Fig. A6b shows a TDE of PS4 with PS1 and subsequent formation of PS8 for HAZ-5. PS4 approaches PS1 at $t_* = 136$ yr with a large impact parameter $b = 3.82$ au compared to the protostellar radius $a_1 = 2.03$ au, and the specific angular momentum becomes temporarily larger (corresponding to $j^2 = 0.028$) than the critical value 0.02 for break-up (see Fig. 13). It is expected that a TDE occurs when a protostar approaches another one within its tidal radius calculated as $r_{\text{tid}} = a_j(m_j/m_i)^{1/3}$, where m_i and m_j are the masses of PS i and PS j , respectively (Rees 1988). Although the impact parameter is larger than the tidal radius (2.30

au), TDE occurs in this case (11th and 12th columns in Tables A1 and A2). Since the masses of PS4 and PS1 are comparable ($m_1/m_4 = 3.82$), both protostars are deformed by each other's tidal force. In the classical theory of TDEs, large mass ratios ($m_j/m_i \gg 1$) have been assumed. In our simulations, the cross-section for the interaction becomes effectively larger than in the case with large mass ratios where only a smaller protostar deforms.

A3 Case without fragmentation

DF occurs for HBZ0 but not for HBZ-6, although the thermal evolution is quite similar in these runs (Fig. 7). Fig. A7 shows the density, temperature, and Toomre Q parameter for HBZ0 and HBZ-6, respectively. For HBZ0, a secondary protostar PS2 forms at $t_* = 4.4$ yr and collides with PS1 at 10.2 yr. PS1 and PS2 have almost equal mass ($0.365 M_{\odot}$ and $0.420 M_{\odot}$, respectively) and about $0.01 M_{\odot}$ of gas is stripped off into the ambient medium after the offset collision. The gas is stretched up to ~ 15 au, and the gas temperature declines adiabatically in the elongated structure. Then unstable spiral arms with $Q < 0.6$ form (lower panels of Fig. A7a).

Contrastingly, for HBZ-6, gas accretion onto the primary PS1 occurs in an almost spherical manner (Fig. 12b). Although multiple protostars form along the filament and collide with PS1, these secondary protostars have small masses ($0.0782 M_{\odot}$, $0.0568 M_{\odot}$, and $0.0389 M_{\odot}$) relative to PS1 ($1.01 M_{\odot}$ at $t_* = 14.4$ yr). Therefore, cool spiral arms do not form as seen for HBZ0. Furthermore, since PS1 continues growing with a high accretion rate ($\dot{M}_* \simeq 0.06 M_{\odot}/\text{yr}$), the circumstellar medium is warm ($T \sim 10^4$ – 10^5 K), and is less susceptible for the gravitational instability (Fig. A7b).

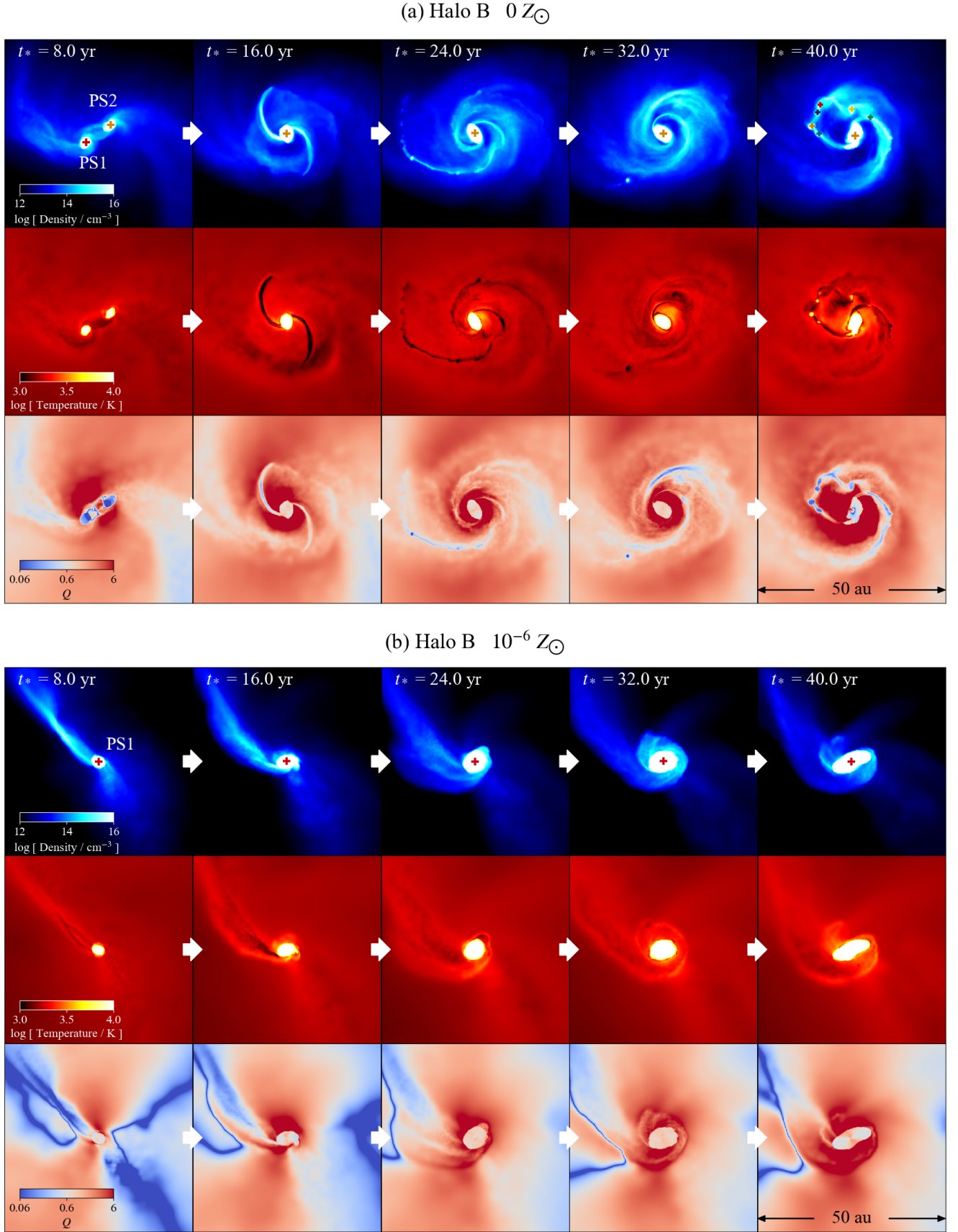


Figure A7. Projections of density (top panels), temperature (middle panels), and Toomre Q parameter (bottom panels) of the accretion discs for (a) HBZ0 and (b) HBZ-6 from $t_* = 8$ to 40 yr.